Strong motion simulations with empirical Green's functions: methodology and application to the 2009 L'Aquila earthquake

Doctorate Program In Seismic Risk
XXVI Cycle

Department of Physics
University of Naples, Federico II

Tutor: Dr. Gaetano Festa

Candidate: Dr. Sergio Del Gaudio

Coordinator of XXVI cycle in Seismic Risk program
Prof. Aldo Zollo

Contents

Introduction 9

1 Earthquake source description 11

1.1 Introduction . . 11

1.2 Earthquake source kinematics . . . 12

1.3 The Representation Theorem . . 17

1.4 The Source Time Function 18
1.5 Source models from strong motion data 20
1.6 High frequency slip description: the K^{-2} model . . . 23

2 Propagation effect: the Green's functions 27
2.1 Introduction . . 27
2.2 The elastodynamic equation 28
2.3 1D and 3D crustal velocity models . 30

2.4 1D velocity models from first arrival time inversion 32
2.5 Empirical Green's functions 47

3 A Case study: the 2009, L'Aquila earthquake 49
3.1 Introduction . . 49
3.2 Geological and seismotectonic context 49
3.3 Strong motion data: mainshock and aftershock analysis 52

3.4 Numerical Green's functions for L'Aquila region 53
3.5 Empirical Green's functions: selection and analysis 53

4 Source inversion of L'Aquila earthquake **59**
4.1 Introduction . . 59
4.2 Data selection . 59
4.3 Model parameterization 60
4.4 Constant rupture velocity inversion 62

4.5 Variable rupture velocity inversion 62

5 Broadband simulations **73**
5.1 Introduction . . 73
5.2 Broadband simulation results . 73
5.3 Broadband simulations with K^{-2} model 75
5.4 Uncertainty due to the EGF selection 79
5.5 Blind simulations 86

Conclusions **93**

Introduction

In the last ten years, thanks to the great advances in computer science and to the huge improvements of strong motion networks, our knowledge of the Earth interior and its related phenomena greatly increased. This improvement directly comes from the amount of collected data, such as recorded signals during earthquakes, that are now shared by worldwide databanks. We observe an earthquake rupture from the elastic waves produced by a sudden release of energy in the Earth's crust: the seismic waves. These waves bring informations on both their source and all the features of the medium that they have passed through. The aim of this thesis was to build up and test a robust methodology to produce synthetic records which are as similar as possible to the real ones. My final goal is to perform ground motion predictions with this technique to obtain scenario simulations for probable future earthquakes in active seismic regions.

To reproduce ground motion, we need to finely model the earthquake source. Since a direct observation is impossible information on seismic source processes is retrieved from data by an inversion procedure. In the first Chapter I discuss in details the representation of the earthquake source and its parameterization. A method to obtain a source model from ground motion records is also presented. Moreover, I discuss a technique to enrich the frequency content emitted by a seismic source.

Along their path, seismic waves are modified by the interaction with the propagation medium, both in amplitude and frequency contents. Reproducing the effect that the propagation has on data is an hard challenge for seismologists. While it is generally possible to model the long-wavelength effect of the geological structure on seismic waves, details still depend on local heterogeneities at small scale. In the second Chapter I illustrate the theory of seismic wave propagation and how it is possible to obtain the medium characteristics from data, in terms of wave velocity distribution as function of depth. I also show how to model the Earth's structure and how to use records of small earthquakes to give a very detailed description of all the features of the propagation medium.

As a case test for the proposed methodology, I investigated the 2009 L'Aquila earthquake. This event of magnitude 6.3 produced hundreds of fatalities and a huge amount of damages which affected L'Aquila city and the surrounding areas. L'Aquila earthquake is also one of the best recorded events of the last years. Moreover we also collected a large number of aftershocks which can be used to obtain information on the propagation medium. For these reasons, this event is a perfect candidate to test the developed method. The chapter three is dedicated to illustrate the characteristics of this earthquake and all the analysis we have done on the selected data.

In the fourth Chapter I apply the technique to obtain a kinematic source model for L'Aquila earthquake and discuss its strengths and weaknesses. Finally, in the last Chapter, I perform ground motion simulations of L'Aquila earthquake and compare them with real observations to test their reliability. After that, I show how to compute "blind" simulations to predict the ground motion of a future earthquake using all the introduced ingredients and test the method applying it again to L'Aquila case.

Chapter 1

Earthquake source description

1.1 Introduction

With the word *earthquake* we refer to a sudden release of energy in the Earth's crust that produces seismic waves. These phenomena are generated by the movements of the tectonic plates that, after their collision produce an increment of the stress along their borders. When the maximum tectonic stress is reached, there is a rapid release of energy causing a relative displacement of two adjacent volumes of rocks, and generating, in this way, a discontinuity surface (fault) between two blocks. In general, dislocations are likely to occur in regions of crustal weakness already broken by previous earthquakes. The rupture initiates on a small nucleation zone where the stress exceeds the static friction between the two blocks, then the friction drops from the static to the dynamic level and the rupture front propagates over the fault surface. From a mathematical point of view the fault is only a "plane", but geologically it is a complex structure with a finite thickness and different types of rocks, that geologists usually indicate as "fault zone".

Generally, we can have two different approaches to the earthquake rupture processes: a kinematic and a dynamic approach. The dynamic approach is formally the best one because it consists in studying the process starting from the physical causes that are responsible of the generation of the fractures. Also, the description of the generation and formation of the seismic waves can be derived from this approach. Unfortunately, it is not a well-posed problem. It requires the definition of the initial values and boundary conditions for the stress necessary for the nucleation and the propagation of the earthquake rupture. For this reason and for the high computational costs, we prefer to use the kinematic approach. From a kinematical point of view, we do not have to investigate the causes that are responsible of an earthquake, but we are interested in the description of its effects, in particular describing the rupture in terms of kinematical variables like relative displacement on the fault and rupture velocity. We are also interested in relate what happens in the fault region to the ground motion recorded at the earth surface. This means that if the displacement discontinuity across a fault is known as a time dependent function of the position on the fault, then the radiated field emitted from the source region is completely determined (Aki and Richards, 2002). In this study we will present the problem of the source kinematics and the role of a detailed kinematic source model to providereliable ground motion simulations.

1.2 Earthquake source kinematics

Let us consider a volume V internal to the Earth, bounded by the surface S. We assume homogeneous boundary conditions on S, which are, for example, representative of the traction-free Earth surface. We indicate with Σ_1 and Σ_2 the two sides of the fault plane that move away from each other, and n is the normal to the fault from Σ_1 to Σ_2 (Figure 1.2.1). During an earthquake, as we said, there is a rupture on the fault plane which can be represented by a dislocation in an elastic medium. This dislocation is defined by the slip vector $\mathbf{\Delta u}$ that is the difference of the displacement between the two sides of a fault with respect to a reference configuration defined at time zero, when the two sides are at their original position. Is it quite obvious that the kinematic quantities (the displacement and its time derivatives) are discontinuous across the surface Σ.

The description of the seismic source can be done at different levels, and this generally depends on the frequency range of interest we are looking to and on the distance from the observation point. Starting from the nucleation zone, close to the earthquake hypocenter, the rupture will propagate over all the fault plane. When reached by the rupture front, each point starts to dislocate and the energy is radiated as elastic waves. The frequency content of these waves is related to medium heterogeneity, to the size of the slip asperity produced by the rupture process and to the velocity at which each point dislocates. In general, we can reasonably assume that the low frequency content of the signal is representative of the whole fault, because a low frequency corresponds to a

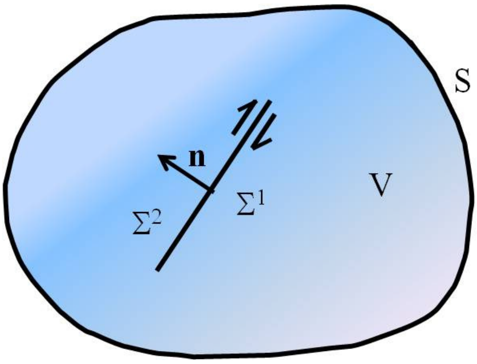

Figure 1.2.1: Representation of a seismic fault as a surface inside a volume V along which slip occurs (Festa and Zollo, 2012).

large wavelength; conversely the high frequency content is representative of the intereference contribution of the different parts of the fault itself. Because of anelastic effects of the rocks, wave attenuation is frequency dependent and is higher for high frequencies. If we are far enough from the fault plane and we consider the low frequency part of the signals, records will be representative of the whole rupture process and it will be impossible for us to appreciate the contribution of the different parts of the fault surface. For this reason, at this level we can approximate the source as a single point. This point souce approximation is useful to estimate the earthquake location and its magnitude. Earthquakes are related to extended rupture surface but, when we locate them, we prefer to consider just one point from which the seismic waves originate. We can imagine this point like the centroid of the fault surface. With *hypocenter*, instead, we indicate the nucleation point of the rupture. If we consider very small earthquakes or we are really far away from the fault region, we are allowed to assume hypocenter as the centroid of the fault. Another macrospopic parameter to introduce is the *seismic monemt*, related to the energy released by the earthquake, which gives us an idea of its "size" and is related to the *magnitude* (that is a logaritmic representation of the moment). This quantity derives from the idea that the dislocation can be described as produced by a couple of forces which produce the relative displacement between the two blocks. This equivalent dynamic model was able to describe the *radiation pattern* of P waves (Figure 1.2.2). The seismic moment can be defined as the moment of

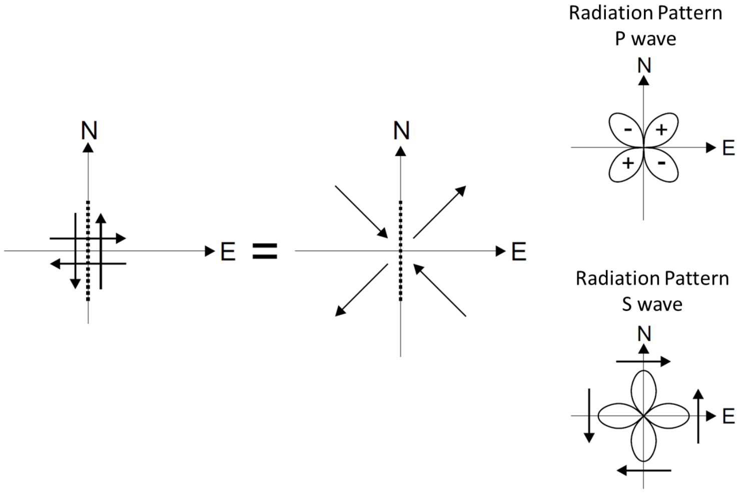
N
E
=
N
E
Radiation Pattern
P wave
N
E
-
+
+
-
Radiation Pattern
S wave
N
E

Figure 1.2.2: Double couple equivalent system for a vertical strike slip fault. The pressure and traction along principal axes is also shown with the relative generated radiation pattern for P and S waves. (Zollo and Emolo, “Terremoti e Onde”)

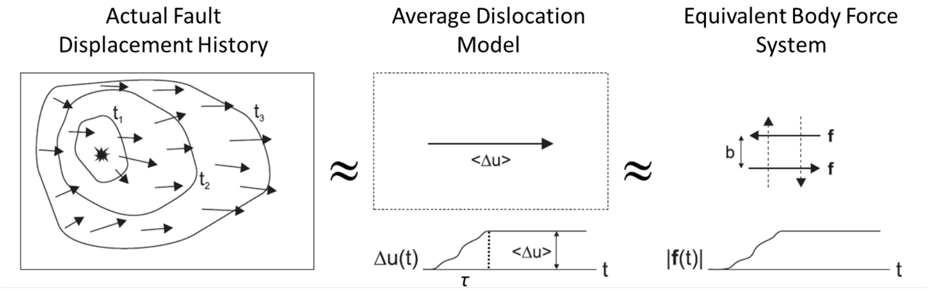

Figure 1.2.3: Approximation of a real rupture process with an equivalent double couple force system (Lay and Wallace, 1995, “Modern Global Seismology”).

this couple:

$$M_0 = \mu < \Delta u\,(t) > \Sigma \tag{1.2.1}$$

where μ is the shear modulus, Σ the fault area and $< \Delta u\,(t) >$ is the mean value of the slip (Figure 1.2.3). Because of the fact that M_0 is not balanced, we should expect the presence of a second couple of forces equal to the first one and with an orthogonal direction. Moreover, the single couple model is not able to explain the S wave radiation pattern, and so in 1960s, with the introduction of three component seismometers and the consequent measure of the complete wave field, the double couple model was definitively accepted. In the far-field approximation, M_0 can be measured considering that it is related to the amplitude of the displacement spectrum in the limit of zero frequency.

Nevertheless, we are often interested in knowing the finite size of the fault plane and the evolution of the rupture propagation. Moreover, the point source approximation is not able to explain the strong ground motion observed in the fault vicinity. For all these reasons, we need to go into details and define a series of parameters useful for the finite source description.

First of all, we have to define the fault dimensions and orientation. The simplest idea is to consider rupture starting from nucleation point and propagateing in all directions. With this idea, fault surface has to assume a circular shape and the radius of this circle can be used to indicate the fault dimension. What in general seismologists prefer, deriving from direct observations in particular of the San Andreas fault (California), is to consider a rectangular fault of length L and width W. San Andreas fault is a strike-slip fault (i.e. a vertical surface of separation between two blocks of rocks) and its longitudinal exten-

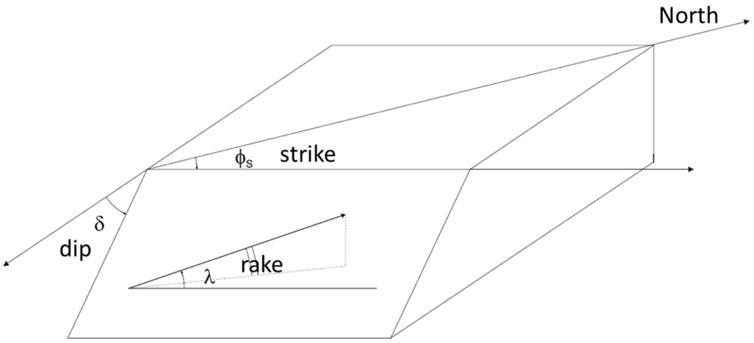

Figure 1.2.4: Representation of fault geometry and spatial orientation (Aki and Richards, 2002, “Quantitative Seismology”).

sion is at least one order of magnitude greater than its vertical width. For this reason, rupture processes related to earthquakes occurring on this kind of fault have a predominant horizontal propagation direction and rectangular geometry is more appropriate to describe this effect. Orientation of the plane is defined by the *focal mechanism*, which consists of three angles: *strike*, *dip* and *rake* (see Figure 1.2.4). The strike is the angle between the direction of the fault length and the north direction; the dip is the angle between the fault width and the horizontal plane; the rake is the average direction of the slip on fault, as comapred to the strike direction.

Rupture evolution is described by its velocity, the *rupture velocity* v_r, the velocity at which the rupture front propagates: if the velocity is homogeneous it can be computed as the ratio betweenthe distance of the fault edge and the nucleation point and the time required to reach that edge. The time at which each point starts to dislocate is the *rupture time* (t_r).

Once reached from the rupture front, the dislocation at a specific point takes time to pass from the initial zero value to the final one, this time is called *rise time* (τ).

1.3 The Representation Theorem

The ground displacement observed at a general location $\mathbf{x}$ on the Earth surface at a time t can be computed using the Betti's reciprocity theorem. It states that a pair of forces applied in a certain volume are related to their corresponding displacements. Starting from this theorem we can derive the *representation integral*: the ground displacement is given by the convolution of the slip function with the elastic response of the propagation medium (e.g. Aki and Richards, 2002)

$$u_m(\mathbf{x},t) = \int_{-\infty}^{+\infty} d\tau \int_{\Sigma} \Delta u_i\left(\vec{\xi},\tau\right) c_{ijkl} n_j \frac{\partial G_{mk}}{\partial \xi_l}\left(\mathbf{x}, t-\tau; \vec{\xi}\right) d\vec{\xi} \qquad (1.3.1)$$

In the above formula c is the fourth-order elastic coefficient tensor and is symmetric with respect to the exchange of all the indices. Due to its simmetry, only 21 of the 81 components are really independent for a general elastic solid medium, but it can be reduced to only two coefficients for an isotropic medium (Jeffreys and Jeffreys, 1972): the Lamé's constants, λ and μ. λ does not have a specific physical meaning, while μ represents the shear modulus of the medium. If our medium is subject to a unit impulse force in space and time, which is mathematically represented by a Dirac delta function, its corresponding displacement is called the Green's function $\mathbf{G}$ and it represents the effect of the propagation of elastic waves in the medium. Specifically, $G_{ij}\left(\mathbf{x}, t, \vec{\xi}\right)$ represents is the i-th component of the displacement recorded at the position $\mathbf{x}$ and at the time t, generated by an unidirectional impulse force acting in the j-th direction at $\vec{\xi}$ at time zero. Using the property of reciprocity of the Green's functions, we can exchange the source and receiver positions and define the quantity

$$T^G_{im}\left(\vec{\xi}, t-\tau; \mathbf{x}\right) = c_{ijkl} \frac{\partial G_{km}}{\partial \xi_l}\left(\vec{\xi}, t-\tau; \mathbf{x}\right) n_j \qquad (1.3.2)$$

that is the Green's traction on the fault plane generated by an impulse force at $\mathbf{x}$ directed along the m-th direction. The boundary conditions across the fault are the continuity of the stressand the discontinuity of the displacement. Moreover, the Green's functions are also continuous through the surface Σ.

In the previous paragraph, we stated that the seismic source can be represented by an equivalent double copuple of forces. We can introduce this assumption in the representation integral 1.3.1 to represent an extended seismic source as a superposition of double-couple point sources. First of all we have to note that only the components of c with $i \neq j$ contribute to the Green's tractions, because the slip vector lies on the fault plane. For an isotropic medium it is possible to show that the observed displacement is independent of the Lamé constant λ. So that, we can rewrite the 1.3.1 as:

$$u_m(\mathbf{x},t) = \int_{-\infty}^{+\infty} d\tau \int_{\Sigma} \Delta u_i\left(\vec{\xi},\tau\right)\mu\left(\frac{\partial G_{mi}}{\partial \xi_j} + \frac{\partial G_{mj}}{\partial \xi_i}\right) n_j d\vec{\xi} \qquad (1.3.3)$$

Remembering that summation over repeated indeces is assumed, by properly changing the indices in the summation, formula 1.3.3 can be also rewritten as:

$$u_m(\mathbf{x},t) = \int_{-\infty}^{+\infty} d\tau \int_{\Sigma} \mu\left(\Delta u_i n_j + \Delta u_j n_i\right) \frac{\partial G_{mi}}{\partial \xi_j} d\vec{\xi} \qquad (1.3.4)$$

The symmetric quantity $\mu\left(\Delta u_i n_j + \Delta u_j n_i\right) = m_{ij}$ has the dimension of a moment per area unit and its integral $\int_{\Sigma} m_{ij} d\vec{\xi}$ is exactly the seismic moment M_0 defined by equation 1.2.1. For our purposes, generally is also convenient to rewrite the representation integral in the frequency domain. The advantage comes from the fact that the displacement can be computed frequency by frequency, we will see that this makes the inversion of band-pass filtered data straightforward.

1.4 The Source Time Function

The slip function may be an arbitrary function of position and time, but has to satisfy three conditions (Festa and Zollo, 2012). The slip modulus must vanish at time zero (no dislocation occurs before the rupture process starts), the modulus of the slip rate tends to zero as the time grows (the rupture cannot continue indefinitely) and the time at which each point on the fault starts to dislocate must satisfy a causality criterion, e.g. the rupture is not allowed to propagate faster than the largest wave velocity in the medium (generally P wave speed for in-plane ruptures and S wave speed for anti-plane ruptures). A simple way to represent Δu is to factorize it in two separate contributions:

$$\Delta u\left(\vec{\xi},t\right) = A\left(\vec{\xi}\right) S\left(t - t_r\left(\vec{\xi}\right); \tau\left(\vec{\xi}\right)\right) \mathbf{r}\left(\vec{\xi}\right) \qquad (1.4.1)$$

where $\mathbf{r}$ is a unit vector that indicates the local direction of the slip (the rake), A is the final amplitude of the slip and the function S describes the slip evolution

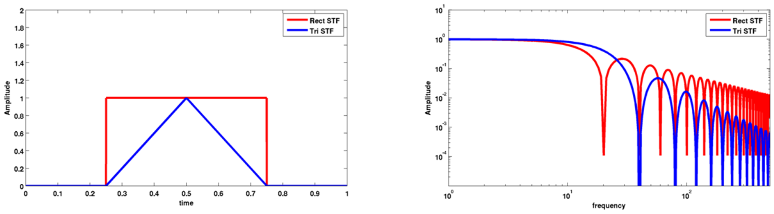

Figure 1.4.1: shape of rectangular and triangular source time function (left) and their amplitude spectra (right)

with time at a specific point of the fault. S has a finite time duration (rise time τ) and is delayed by the rupture time t_r. The time derivative of S, the slip velocity time function, is generally known as the source time function (STF) (Aki and Richards, 2002). It is important to define the *source time function*(STF), that describe the way in which the point reaches its final slip value. The shape of the STF has an important effect on ground motion simulations because controls the high frequency part of the signals. Several authors have proposed different functional forms for the STF (Fukuyama and Irikura, 1986; Fukuyama and Mikumo, 1993; Cotton and Campillo, 1995) and have pointed out the importance of the STF in kinematic source models for strong motion prediction (Hisada, 2000, 2001; Guatteri et al. 2003). In this thesis we are going to use the two simplest functions: a rectangle and a triangle functions. As said, their expression in frequency domain has an effect on the strong motion simulations, expecially at high frequency. In frequency domain we can define rispectively this two STFs with the equations

$$S_r\left(\omega,\tau\right)=\frac{\sin\left(\omega\frac{\tau}{2}\right)}{\omega\frac{\tau}{2}}e^{-i\omega\frac{\tau}{2}} \tag{1.4.2}$$

$$S_t\left(\omega,\tau\right)=\frac{\sin^2\left(\omega^2\frac{\tau^2}{4}\right)}{\omega^2\frac{\tau^2}{4}}e^{-i\omega\frac{\tau}{4}} \tag{1.4.3}$$

Both these STFs are *sinc* functions (sine wave that decays in amplitude as $^1/_x$) with a phase shift that depends on the rise time. The shape of 1.4.2 and 1.4.3 is shown in Figure 1.4.1, they have a plateau at low frequencies and a decay for frequency larger than cut-off frequency.

1.5 Source models from strong motion data

It is impossible to have direct observation on what happen in the fault zone during an earthquake so that, the only way to obtain information about the source and source parameters is by inverting strong motion records. Generally, what we want to retrieve is the slip function and, to do that, we need an appropriate parameterization. Starting from the representation theorem, we assume that the Green's tractions are known. In practice, the inverse problem consists in the determination of the slip function through the estimation of the final slip, the rupture times, the rise time and the slip direction. The shape of the STF generally is assumed a-priori to reduce the number of the unknowns of the inverse problem. The first study, in which the problem of the slip determination was considered on the formal basis of the linear inverse theory, was published by Olson and Apsel (1982). This study was based on a matrix version of the representation integral and two methods for the solution of the inverse problem were presented: the least-square method, which minimizes the squared differences between simulated and observed data, and the constrained least-squares method, which simultaneously includes a set of linear inequalities. During the last ten years, the great progress of computer science, has led many seismologists to face the source inversion problem in its complete non-linear formulation.

Intuitively, the best way to limit the number of parameters is to subdivide the fault plane in large areas where the parameters are assumed constant. These areas are denoted as *subfaults*. The size of the subfault is related to the minimum wavelength resolved by the data and the parameters grid in the inverse problem is generally one order of magnitude coarser than the discrete grid used in the computation of the forward problem. We have two possibilities: we can define a set of n parameters for each subfault (if we have m subfaults, the total number of parameters is $n_p = m \times n$) or we can define the parameters for n_c control points and then make an interpolation for the rest of the grid. In the last case, an interpolating function has to be chosen. Denoting with $\mathbf{m}$ the set of parameter to determine, for a certain point on the fault plane $\vec{\xi}$ the respective values of parameters are:

$$m_j\left(\vec{\xi}\right) = I\left(\vec{\xi}; m_{1j}, m_{2j}, ..., m_{n_c j}\right) \qquad j = 1, ..., n \tag{1.5.1}$$

where I is the interpolating function (e.g. a bilinear Lagrange interpolator or by a bicubic spline function). Interpolation is chosen usually to have smoother representation instead of the constant cell parameterization (Figure 1.5.1). Rupture times are the most problematic parameters in kinematic inversions, because it

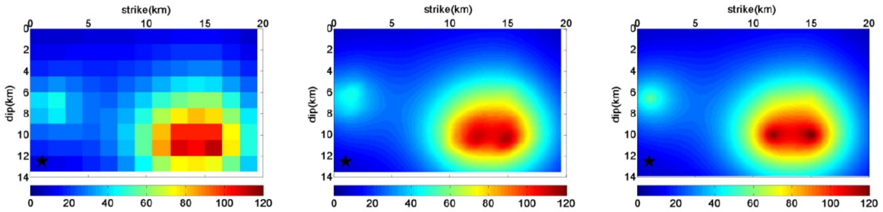

Figure 1.5.1: The same slip map represented by different parametrizations. On the left, a constant cell discretization, in the middle, a bi-cubic spline interpolation based on control nodes, on the right a superposition of overlapping Gaussian functions. The two smooth images are very similar, with differences related to the shape of the singularities (Festa and Zollo, 2012).

is difficult to impose the causality condition between contiguous regions of the fault (Cotton and Campillo, 1995). For this reason we prefer to replace them by rupture velocities using the *eikonal equation*

$$|\nabla t_r| = \frac{1}{v_r} \tag{1.5.2}$$

The positivity constraint of rupture velocity intrinsically assume the causality in rupture propagation.

In this study we describe of the kinematic inversion strategy proposed by Lucca et al. (2012) based on a two step approach. An application of this method is shown in a following section. The ground motion recorded at a seismic station non linearly depends on the kinematic rupture history, in terms of slip and rupture velocity. However, for a fixed rupture velocity distribution, the representation integral is linear with respect to the final slip that could be retrieved by a regularized linear inversion of strong-motion data. Although the rupture velocity is unlikely to be known a-priori, we can still take advantage from the linearity by separating the inverse problem into two nested problems. Let's consider the representation integral written in a very simple way

$$\mathbf{u} = K\left(\mathbf{V_r}, \mathbf{U}\right) \tag{1.5.3}$$

where K is an operator that includes the product by the Green's tractions and integration on the fault plane. For a fixed $\mathbf{V_r}$, K is linear with respect to the slip $\mathbf{U}$ and we can solve the problem assuming as misfit function the L_2 norm

$$\left\|\mathbf{u} - K\left(\mathbf{V_r}, \mathbf{U}\right)\right\|^2 \tag{1.5.4}$$

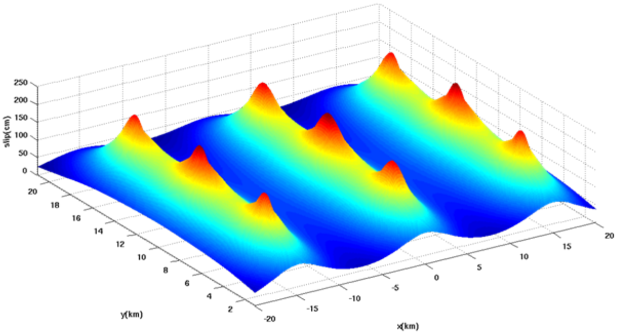

Figure 1.5.2: Example of slip distribution obtained by overlapping of 2D Gaussian functions.

More precisely, the full inverse problem is solved by a two step iterative procedure. During the first step, we fix a $\mathbf{V_r}$ distribution, and the linear problem is solved with a Non Negative Least Square (NNLS) algorithm (Lawson, C.L., Hanson, R.J., 1974). We solve the non-linear problem to search the $\mathbf{V_r}$ map using the global search given by the Neighbourhood algorithm (Sambridge, 1999; 2001), which minimizes the misfit function. For each distribution of $\mathbf{V_r}$, we find the slip map that minimize the associated linear problem. The procedure stops when the misfit value is below a given threshold. Specifically, we describe the slip as a superposition of overlapping 2D Gaussian functions (Figure 1.5.2) $\phi_i\left(\vec{\xi},\vec{\xi_i}\right) = e^{-\frac{1}{\sigma^2}\left(\vec{\xi}-\vec{\xi_i}\right)^2}$ centered in $\vec{\xi_i}$ and of width σ. In frequency domain this slip distribution can be written as

$$\phi\left(\vec{\xi},\omega\right) = \sum_{i=1}^{n} A_i \phi_i\left(\vec{\xi},\vec{\xi_i}\right) \tag{1.5.5}$$

Considering the Gaussian functions equally spaced over the fault plane, their number is chosen fixing the amount of overlapping $\chi = \frac{\sigma}{\Delta\xi}$, where $\Delta\xi$ is the distance between two close centers. It can be shown that a minimum condition for the χ parameter is that it has to be at least greater than $1/\pi$ (Lucca et al., 2012). Rupture velocity is discretized in cells where the value is constant and described by a piecewise bilinear function. The misfit function is the normalized

L^2 norm between real data and computed synthetics in the frequency domain:

$$\varphi(\omega) = \sum_{i=1}^{n_{sta}} \sum_{j=1}^{3} \sum_{k=1}^{n_\omega} |u_{ijk}^{synt} - u_{ijk}^{obs}|^2 \qquad (1.5.6)$$

where n_{sta} is the number of station we have selected for the inversion, n_ω is the number of frequencies (it depends of the frequency band chosen with respect to the minimum resolvable wavelength). The index j refers to the three components of the displacement vector. The Parseval theorem warrants that the L^2 norm in the time domain is the same as in the frequency domain (apart from a constant factor depending on the definition of the Fourier transform). Often we prefer to use this latter because the dimension of a timeseries is of the order of $10^3 - 10^4$, while the dimension of a band-limited Fourier series is on average two orders of magnitude smaller.

The advantage of using the Neighbourhood algorithm is that, instead of converging to a single minimum, it points to several regions where the global minimum can be located. Such an algorithm, hence, is well suited for ill-posed problems, such as the kinematic inversion, where the solution may not be unique. At each stage, the entire parameter space is partitioned into a set of *Voronoi cells* (nearest neighbour regions, as defined by a suitable norm), one associated with each previously sampled model. A Voronoi cells of a particular model is a polygon whose interior consists of all points in the parameter space which are closer to this particular model than to any other model. Between consecutive iterations, the new sample is recalculated in only the Voronoi cells of the previous models having the smallest misfit (Figure 1.5.3). For this reason this technique is computationally more convenient than a standard *Montecarlo* exploration. Moreover, this algorithm requires the set of only two parameters, which control the process: the number of initial points and the number of re-sampled cells.

1.6 High frequency slip description: the K^{-2} model

One of the problem of the kinematic inversion lies in the fact that it is band limited in frequency. In the next Chapter, we will show how the Green's funtion are related to our degree of knowledge of the propagation medium. It is important to say that the maximum resolvable frequency on data (through the computation of synthetics) depends on the Green's function frequency content. Since high frequency corresponds to small wavelengths, knowing the Green's functions up to high frequency implies a very detailed knowledge of the propagation medium.

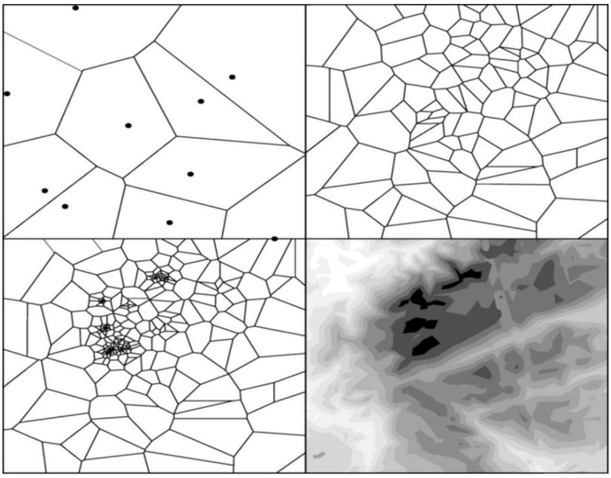

Figure 1.5.3: Example of exploration for two parameters problem. The upper-left panel shows 10 samples and the corresponds Voronoi cells; the upper-right panel shows 100 samples. The lower-left panel similar to upper-right panel but with 10000 samples. Here the algorithm concentrates on four distinct region corresponding to the minimum of the misfit. The lower-right panel shows the contours of the misfit function in grey scale.

Generally, we are interested into the kinematic inversion that works with low frequency data. Therefore, modelling realistic time histories, expecially high frequency accelerations, is of great importance for determining, for example, the structural response of building or for giving damage estimations. Looking at ground displacement, we know that the amplitude spectra can be approximated by a flat level (controlled by the seismic moment) for $\omega < \omega_c$ and with a decay $\propto \frac{1}{\omega^2}$ for $\omega > \omega_c$, where ω_c is called *corner frequency.* At low frequencies we observe the effect of the whole fault plane, the radiation is coherent and the amplitude spectrum results in a plateau. Above the corner frequency we observe the contribution of small wavelengths that comes from the different parts of the fault with different phases, the radiation becomes incoherent and results in a sort of destructive interference which produces the slip decay. Starting from this assumption and considering the slip spectrum in the wavenumber domain $k = \frac{2\pi}{\lambda}$, several authors (Herrero and Bernard, 1994; Gallovic and Brokesova, 2004) have proposed a genral model for slip spatial spectrum, so called $k-square$ model

$$\Delta u\left(k\right) = C\frac{\Delta\sigma}{\mu}\frac{L}{k^2} \tag{1.6.1}$$

Its low wavenumber content is controlled by the seismic moment, and its high wavenumber decay exponent results from an assumed and plausible self-similarity of the slip distribution. C is a geometrical factor, $\Delta\sigma$ is the stress drop, μ is the rigidity of the medium and L is the fault length. $k - square$ models give a realistic description of the slip amplitude spectrum, but the phases are generally assumed to be random (except for the very first terms at low wavenumber for which we can, for example, fix the distribution obtained by a kinematic inversion).

In this work we will present results obtained using and developing the approach presented by Causse et al. (2009) to model high frequency slip function. The static slip distribution in the wavenumber domain is described by an asymptotic k^{-2} decay beyond the corner wavenumber $k_c = {}^{K}\!/_{L}$, where K is a non-dimensional parameter that controls the degree of roughness of the slip heterogeneity. The rupture process is modelled as a slip pulse of width L_0 propagating at constant rupture velocity (Figure 1.6.1). The rise time is assumed to be constant, $\tau = \frac{L_0}{v_r}$, for $k < {}^{1}\!/_{2L_0}$, and inversely proportional to k for higher wavenumbers. Unlike classical $k - squake$ models, in this approach small scale slip heterogeneities are assumed to have random rupture directions, this choice strongly reducing directivity effect at high frequency. The high wavenumber slip is composed of a set of heterogeneities of different scales, considered as independent subevents. These subevents start to dislocate as the main rup-

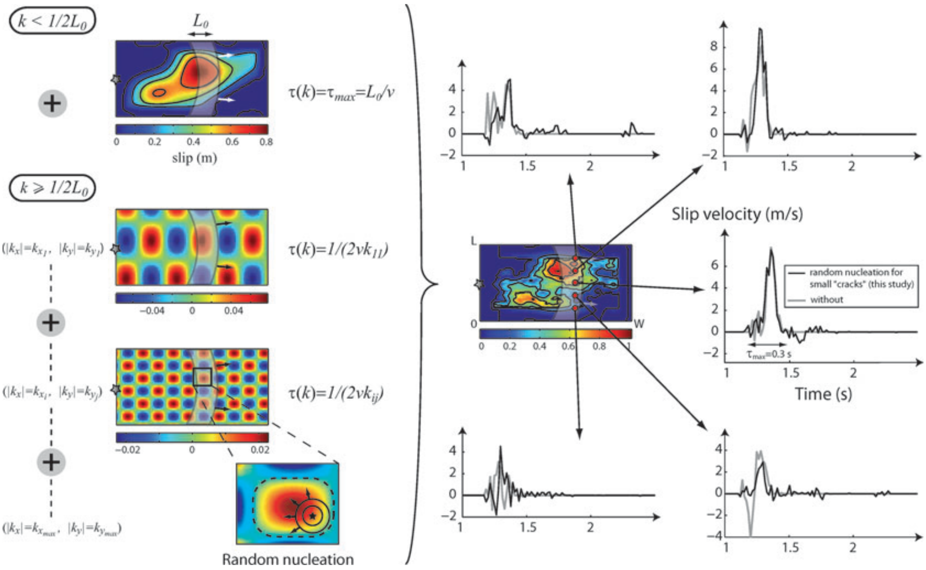
k < 1/2L0
L0
τ(k)=τmax=L0/v
slip (m)
k ⩾ 1/2L0
τ(k)=1/(2vk11)
τ(k)=1/(2vkij)
Random nucleation
Slip velocity (m/s)
random nucleation for small "cracks" (this study)
without
τmax=0.3 s
Time (s)

Figure 1.6.1: Representation of the rupture process, modelled as a slip pulse propagating at constant rupture velocity v. The figure also displays example of resulting STFs, compared with the functions that would be obtained from a classical k^{-2} model (without random nucleation points). (Causse et al., 2009)

ture front reaches one point, randomly chosen, from which a secondary rupture front propagates. The slip duration for a given subevent is proportional to its wavenumber. The final static slip distribution results from the superposition of a "deterministic" part ($k \leq k_c$) and of a purely "stochastic" part ($k > k_c$). Phases are completely random for high wavenumbers but, for the deterministic part, we consider them fixed in a way to obtain a large slip path placed in the center of the fault plane. There is, also, the possibility to fix this deterministic slip distribution including what we have obtained from a kinematic source inversion. In the following Chapters we will discuss if and how the use of a specific source model affect the simulations.

Chapter 2

Propagation effect: the Green's functions

2.1 Introduction

As we have seen in the previous Chapter, the displacement recorded at the Earth surface can be expressed as the convolution of the source function by the Green's tractions using the representation theorem. Because of such a linear coupling, the determination of the source parameters from the recorded seismograms requires an accurate modeling of the propagation effects down to the wavelengths at which we can resolve the rupture history. A complete description of the propagation medium requires the knowledge of the spatial distribution of the density, the P and S wave velocities and the anelastic attenuation parameters. Smooth wave velocity and attenuation models are generally derived from the tomographic inversions of first arrival-times of local earthquake records (we will explain later in detail this approach). In most cases, the best available model of the propagation medium is one-dimensional, which can satisfactorily represent the low frequency propagation of seismic waves up to the surface. 1D models, however, may be inadequate to describe the seismic wavefield in the case of dominant 3D effects perturbing the amplitude and the phase of the seismic waves, such as the presence of basins or strong lateral heterogeneities. In several active seismic areas, which are well monitored, 3D models are available with a space resolution varying from few hundreds of meters to few kilometers, allowing for a more reliable computation of the Green's functions. We have to note that the inaccuracy in modeling the propagation effects introduces uncertainties in the rupture description and in the estimation of the source parameters. Such an uncertainty is difficult to be assessed since the true propagation model is unknown and the errors on the velocity model and on the location and morphology of the interfaces non linearly affect the Green's tractions computation. Several studies have shown that source models derived from the waveform inversion are strongly sensitive to the wave propagation (Graves, R.W., Wald, D.J., 2001; Liu, P., Archuleta, R.J., 2004). Even when inverting synthetic waveforms the data misfit may rapidly degrade, when replacing the 3D true model with its best 1D approximation, and the estimations of the relative source parameters are strongly sensitive to the considered Earth model.

2.2 The elastodynamic equation

The description of fault mechanics is based on the solution of the fundamental elastodynamic equation, derived from the classical Newtonian representation. This fundamental equation relates the forces in the medium to the measurable displacement. It is inferred from the second law of dynamics for continuous media:

$$\rho\ddot{\mathbf{u}} = \mathbf{f} + \nabla \cdot \sigma \tag{2.2.1}$$

where ρ is the density of the solid body, $\ddot{\mathbf{u}}$ is the time second derivative of the displacement, that is related to the deformation of the body, $\mathbf{f}$ is the applied external body force density acting per volume unit, and finally σ the stress tensor. Experimentally Hooke observed that the extension of a spring linearly increases with the applied load. This is the simplest representation of an elastic constitutive law, which for a continuous system corresponds to a linear relation between stress and strain; for the components we have:

$$\sigma_{ij} = c_{ijkl}\varepsilon_{kl} \tag{2.2.2}$$

c_{ijkl} is the elastic coefficient tensor introduced before, while ε_{kl} is the symmetric strain tensor

$$\varepsilon_{kl} = \frac{1}{2}\left(\frac{\partial u_k}{\partial x_l} + \frac{\partial u_l}{\partial x_k}\right) \tag{2.2.3}$$

For an isotropic medium c depends only on the Lamé constants, $c_{ijkl} = \lambda\delta_{ij}\delta_{kl} + \mu\left(\delta_{ik}\delta_{jl} + \delta_{jk}\delta_{il}\right)$, and substituting 2.2.2, 2.2.3 and the definition of c in the 2.2.1 we obtain:

$$\rho\frac{\partial^2 u_i}{\partial t^2} = f_i + (\lambda + \mu)\frac{\partial}{\partial x_i}\frac{\partial u_j}{\partial x_j} + \mu\frac{\partial}{\partial x_j}\frac{\partial u_i}{\partial x_j} \tag{2.2.4}$$

Going back to the vectorial form and using the property of the vectorial product, we find the *elastodynamic equation*:

$$\rho\frac{\partial^2\mathbf{u}}{\partial t^2}=\mathbf{f}+(\lambda+2\mu)\nabla(\nabla\cdot\mathbf{u})-\mu\nabla\times\nabla\times\mathbf{u} \tag{2.2.5}$$

From this equation we can derive two wave equations, the first for an irrotational field (P wave) and the second for a solenoidal field (S wave):

$$\nabla\times\mathbf{u_p}=\mathbf{0}\implies\frac{\partial^2\mathbf{u_p}}{\partial t^2}=c_p^2\nabla^2\mathbf{u_p} \tag{2.2.6}$$

$$\nabla\cdot\mathbf{u_s}=0\implies\frac{\partial^2\mathbf{u_s}}{\partial t^2}=c_s^2\nabla^2\mathbf{u_s} \tag{2.2.7}$$

where $c_p=\sqrt{\frac{\lambda+2\mu}{\rho}}$ and $c_s=\sqrt{\frac{\mu}{\rho}}$ are the P and S wave velocities.

In equation 2.2.5 $\mathbf{f}$ represents the source contribution. Assuming it as a unidirectional impulse force, $\mathbf{f}=\delta(\mathbf{x})\,\delta(t)\,\mathbf{e_j}$, we can obtain a solution for an isotropic and homogeneous unbounded medium, that is the relative displacement produced by this force

$$u_i(\mathbf{x},t)=\frac{1}{4\pi\rho c_p^2 r}\gamma_i\gamma_j\delta\left(t-\frac{r}{c_p}\right)+\frac{1}{4\pi\rho c_s^2 r}(\gamma_i\gamma_j-\delta_{ij})\,\delta\left(t-\frac{r}{c_s}\right)+$$
$$\frac{1}{4\pi\rho r^3}(3\gamma_i\gamma_j-\delta_{ij})\int_{r/c_p}^{r/c_s}\tau\delta(t-\tau)\,d\tau \tag{2.2.8}$$

where $\gamma=\frac{\mathbf{x}}{r}$ are the director cosines of the position $\mathbf{x}$ and r is the source-receiver distance. This displacement is exactly the elastodynamic Green's function and is made of three terms. The first two, which decrease with the inverse of the distance are the contributions of the P and S waves, that we refer to as *far field*. The third one is the so called *near field*, which has a more rapid decrease with the distance ($\propto {}^1\!/_{r^2}$). The far field terms show a dependence on a time delay typical of a pertubation that propagates and they clearly represent the P and S waves. Moreover, if we look at the director cosines, their polarization is fixed: P-wave term oscillates in the propagation direction, while S-wave term is polarized in a plane orthogonal to the propagation direction. Conversely, near field has a undefined polarization because results from a composition of P and S waves. According to its expression, the relative predominance of near and far field terms is related to the observation distance. In reality, if we consider the equation 2.2.8 in frequency domanin, we see that the relative amplitudes

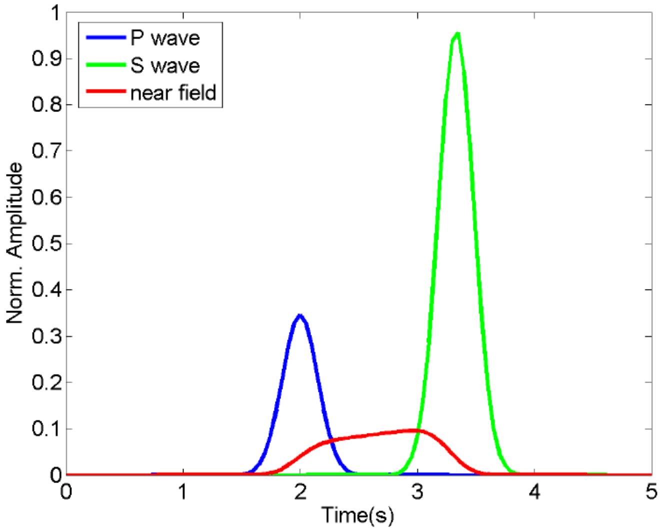

Figure 2.2.1: P-wave, S-wave and near field computed for: $r = 10km$, $c_p = 5km/s$, $c_s = 3km/s$, $\rho = 2.5g/cm^3$, $\gamma_i = \gamma_j = \frac{1}{\sqrt{2}}$.

are also frequency (or wavelength) dependent. Generally, near field is dominant for distances less than one wavelength, while far field terms are dominant for distances greater than few wavelengths. In Figure 2.2.1 is shown an example of these three contribution to the Green's function.

2.3 1D and 3D crustal velocity models

Parametrizing the Earth crust structure as a layered medium is generally appropriate, since the elastic proprieties of the Earth mainly change with depth due to sedimentation, compaction and thermal processes. The importance of finding a reliable, 1-D reference velocity model has been emphasized by many authors (Crosson 1976; Thurber 1983; Kissling et al. 1995). 1D velocity models are routinely used in seismic network operations and in seismological studies to estimate earthquake location, focal mechanisms and other seismic source parameters.

Several techniques are widely used for the computation of the Green's tractions providing the response of a 1D medium. For horizontally layered media, the reflectivity method (Kennett and Kerry, 1979; Müller, 1985) solves the wave equation in the frequency-wavenumber domain by propagator matrix techniques, which account for the continuity of displacements and tractions at the model interfaces. Reflectivity can be efficiently coupled with the discrete wavenumber decomposition of the Green's functions (Bouchon, 1981). Such an approach was implemented in the code AXITRA (Coutant, 1989). With minor variations, the same ideas were also implemented in the frequency-wavenumber integration code (FK) of Zhu and Rivera (2001). The discrete wavenumber finite element integration (Olson, A.H., Orcutt, J.A., Frazier, G.A., 1984) becomes computationally competitive and possibly faster than the above methods when the velocity varies smoothly with depth. To accurately describe a linear increase of velocity with depth, in fact, reflectivity techniques have to decompose the model into a large number of very thin layers, with thickness smaller than the wavelengths of interest. The finite element integration method is efficiently implemented for the evaluation of strong motion data from a finite fault in the COMPSYN code (Spudich and Xu, 2003).

Several full 3D computational methods and codes are available for the evaluation of the Green's tractions in complex geological structures such as the finite-differences method (Graves, 1996; Moczo et al., 1999), the spectral element methods (Komatitcsh and Vilotte, 1998; Chaljub et al., 2007) and the discrete Galerkin methods (Dumbser and Käser, 2006). As compared to 1D models, the computation of a seismic wavefield using a 3D structure still remains expensive and in many cases prohibitive for building up a Green's functions archive, usable for example during an inversion procedure. The computation can be improved using the reciprocity of Green's functions as done for the definition of the Green's traction in equation 1.3.2. If n_s is the number of sources and n_r the number of receivers, the direct computation of Green's tractions requires n_s runs, if we fix the focal mechanism, and $2n_s$ runs, when the slip direction is not assumed a-priori. Using the reciprocity we can directly evaluate the tractions on the fault as the superposition of the signals provided by three orthogonal impulse sources located at each receiver, with $3n_r$ runs. Since the number of receivers is generally smaller (few to several tens of stations) than the number of sources (several hundreds to many thousands depending on fault discretization) the reciprocity is preferred to reduce the computational cost of the Green's tractions evaluation.

A complete wavefield modeling is generally required for the interpretation of surface waves, which are sensitive to the shallow structure of the Earth and its lateral variations, and of body waves at regional distances, because the ray paths inside the crust and the upper mantle can be complex. For this goal, teleseismic Green's functions can be obtained using full 3D propagation methods in a realistic Earth model, which includes the crust, the oceans and the topography. To do that, Spectral Element Method (SEM) codes are available and widely used. For geophysical pourpose, the SEM is probably the best way for modelling 2D and 3D wave propagation in heterogeneous media. The method combines main advantages of finite element with the spectral methods based on algebraic polynomials in space (Chebichev or Legendre). This method is more expensive than classical finite differences, but it provides much higher accuracy.

2.4 1D velocity models from first arrival time inversion

Since in many cases 1D models represent a good approximation of Earth structure, generally we are interested in obtain this kind of description of the propagation media. Most velocity models of the Earth's interior are derived by first establishing a simple smooth model that explains on average the observations. Subsequently, this initial model is modified until a sufficient degree of coincidence between the observations and predicted values is reached. Many authors (e.g. Kissling et al. 1994) proposed a method to obtain a the best 1D model by inverting travel time data. The determination of this model is, generally, a trial and error process that ideally starts with the collection and selection of a priori information about the subsurface structure. Since this process can lead to ambiguous results, particularly when more than one a priori 1D models have been established, several parameters that control the inversion need to be varied and the corresponding results need to be evaluated. In particular, part of this work has been dedicated to solve the problem of the determination of 1D continuous velocity model through the non-linear inversion of first P arrival times. We implemented an algorithm that, given the mesured P arrival times for each receivers, calculates the best velocity model through the downhill SIMPLEX inversion method (Nelder and Mead, 1965).

2.4.1 The ray theory

In classical optics, the geometry of a wave surface is governed by Huygens' principle, which states that every point on a wavefront can be considered the source of a small secondary wavelet that travels outward in every forward direction with the velocity of the medium at that point;, given the location of a wavefront at a certain time, we can predict future positions of the wavefront. It's clear that there is a temporal dependence in the shape of the wavefront. Because rays are the normal to the wavefront, the rays will also change with time. Fermat's principle governs the geometry of raypaths. This usually means that the ray will follow a $minimum - time$ path to move from a point A to a point B.

Starting from a scalar wave equation like (2.2.6) or (2.2.7) and making a Fourier Transform, we can obtain the Helmoltz's equation

$$\nabla^2 s\left(x,\omega\right)+\frac{\omega^2}{c^2\left(x\right)}s\left(x,\omega\right)=0 \tag{2.4.1}$$

where we now suppose that the wave velocity is a function of x. In high frequency approximation ($\omega \to \infty$), a possible solution of the equation (2.4.1) is

$$s\left(x,\omega\right)=s_0\left(\omega\right)A_0\left(x\right)e^{-i\omega T(x)} \tag{2.4.2}$$

where s_0 is the source term, T is the travel time from the source to the reciver and A_0 is the wave amplitude (T and A_0 are independent from ω). Replacing the (2.4.2) in the (2.4.1), we obtain the *Eikonal equation*

$$\left(\boldsymbol{\nabla}T\right)^2-\frac{1}{c^2}=0 \tag{2.4.3}$$

that describe the propagation of a wavefront and so from the (2.4.3) is possible to reach the equation of the ray path. If we consider the wavefront for a given time $t_0 = T$, for a subsequent time $t_1 = T + dT$ the wavefront has reached new points and so has a new surface. Note that

$$t_1-t_0=dT=\frac{\partial T}{\partial x}dx+\frac{\partial T}{\partial y}dy+\frac{\partial T}{\partial z}dz=\boldsymbol{\nabla}T\cdot d\mathbf{r} \tag{2.4.4}$$

with $d\mathbf{r} \equiv (dx, dy, dz)$. The quantity $\boldsymbol{\nabla}T$ has, by definition, the direction of the normal at the surface with same value of T. If $r\left(s\right)$ represents the position along the ray path, it has the same direction of $\boldsymbol{\nabla}T$, moreover the components of the vector $\frac{d\mathbf{r}}{ds}=\left(\frac{dx}{ds},\frac{dy}{ds},\frac{dz}{ds}\right)$ represent the direction cosines of the ray and then

$$\frac{d\mathbf{r}}{ds}=k\boldsymbol{\nabla}T \tag{2.4.5}$$

furthermore

$$\frac{d\mathbf{r}}{ds}\cdot\frac{d\mathbf{r}}{ds}=\left(\frac{dx}{ds}\right)^2+\left(\frac{dy}{ds}\right)^2+\left(\frac{dz}{ds}\right)^2=1 \tag{2.4.6}$$

and rewriting the (2.4.6) using the (2.4.5) we obtain

$$k^2 \left[\left(\frac{\partial T}{\partial x} \right)^2 + \left(\frac{\partial T}{\partial y} \right)^2 + \left(\frac{\partial T}{\partial z} \right)^2 \right] = k^2 \left(\boldsymbol{\nabla} T \right)^2 = 1 \tag{2.4.7}$$

and using the eikonal equation (2.4.3), results

$$k^2 \left(\boldsymbol{\nabla} T \right)^2 = k^2 \frac{1}{c^2} = 1 \Longrightarrow k^2 = c^2 \tag{2.4.8}$$

finally we can write

$$\frac{d\mathbf{r}}{ds} = c \boldsymbol{\nabla} T \tag{2.4.9}$$

deriving this we arrive at the raypath equation (in general we have to consider that c is a function of $\mathbf{r}$)

$$\frac{d}{ds} \left[\frac{1}{c\left(\mathbf{r}\right)} \frac{d\mathbf{r}}{ds} \right] = \frac{d}{ds} \boldsymbol{\nabla} T = \boldsymbol{\nabla} \left(\frac{1}{c\left(\mathbf{r}\right)} \right) \tag{2.4.10}$$

We can obtain some insight into the physics of (2.4.10) by considering a simple example. If we follow a ray through a material that has a change in velocity in only one direction, say depth ($c = c\left(z\right)$), then $\boldsymbol{\nabla} \frac{1}{c} = \frac{\partial}{\partial z} \left(\frac{1}{c(z)} \right)$ and

$$\frac{1}{c} \frac{dx}{ds} = c_1 = const. \qquad \frac{1}{c} \frac{dy}{ds} = c_2 = const. \tag{2.4.11}$$

The ratio of c_1 to c_2 confines the raypath to a plane that is normal to the xy plane. (In other words, the projection of the ray into the xy plane is a straight line.) For convenience, and without loss of generality, we can choose this plane to coincide with the xz plane. At a given point the direction cosine of the ray are given by

$$\frac{dx}{ds} = \sin i \qquad \frac{dz}{ds} = \cos i \tag{2.4.12}$$

thus

$$\frac{1}{c} \frac{dx}{ds} = \frac{\sin i}{c} = const. = p \tag{2.4.13}$$

The constant p is called the *ray parameter*, or horizontal slowness, p varies from 0 (vertical travel path) to $1/c$ (horizontal travel path). The angle i is called the *angle of incidence*, and it gives the inclination of a ray measured from the vertical (z direction) at any given depth. For a prescribed reference point and

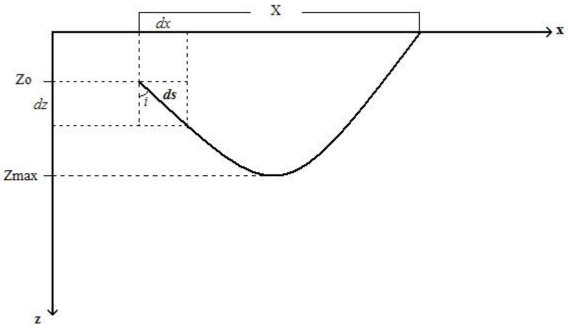

Figure 2.4.1: Geometry of the ray segment ds, along a path from a source to a surface receiver. The velocity of the medium varies only along the z direction, so there will be symmetry of downgoing and upgoing legs of the raypath.

takeoff angle, a ray will have a constant ray parameter, p, for the entire path. Equation (2.4.13) is also known as Snell's law. Now let us consider

$$\frac{d}{ds}\left(\frac{1}{c}\frac{dz}{ds}\right) = \frac{d}{dz}\frac{1}{c} \tag{2.4.14}$$

It's simple to prove that

$$\frac{di}{ds} = p\frac{dc}{dz} \tag{2.4.15}$$

Equation (2.4.15) states that the curvature of a ray is directly proportional to the velocity gradient (dc/dz). If velocity increases with depth, then the ray curves upward. If velocity decreases with depth, then the ray curves downward. For a given source-receiver geometry several possible connecting raypaths may exist, which means that a multiplicity of arrivals will occur, all with different initial angles and travel times. Consider the Fig. (2.4.1). At any point along the travel path we have

$$\sin i = \frac{dx}{ds} = cp$$
$$\cos i = \frac{dz}{ds} = \sqrt{1-\sin^2 i} = \sqrt{1-c^2p^2}$$
$$\Downarrow$$
$$dx = ds \sin i = \frac{dz}{\cos i} cp = \frac{cp}{\sqrt{1-c^2p^2}} dz \tag{2.4.16}$$

eq. (2.4.16) can be integrated over the depth range traversed by the ray to give the distance $X(p)$, at which a ray with ray parameter p will emerge:

$$X(p) = \int_{z_0}^{z_{max}} \frac{cp}{\sqrt{1-c^2p^2}} dz + \int_{z_{max}}^{0} \frac{cp}{\sqrt{1-c^2p^2}} dz \tag{2.4.17}$$

where z_{max} is the maximum depth of penetration (also called the turning point of the ray). The time it takes for the ray to arrive is obtained similarly:

$$dT = \frac{ds}{c} \Longrightarrow T(p) = \int_{z_0}^{z_{max}} \frac{1}{c\sqrt{1-c^2p^2}} dz + \int_{z_{max}}^{0} \frac{1}{c\sqrt{1-c^2p^2}} dz \tag{2.4.18}$$

where T is the travel time along the raypath to the distance defined by eq. (2.4.17).

2.4.2 Formulation of the inverse problem

In this work we prefer to move from the space-time domain to the $\tau - p$ domain. The inversion in $\tau - p$ domain is extensively used in 1D problems. The parameter τ, introduced by Gerver and Markushevich (1966), is defined as:

$$\tau = T - pX \tag{2.4.19}$$

This quantity represents the intercept time with the $X = 0$ axes of the tangent at the $T = T(x)$ curve in X and with slope p. Since equations 2.4.17 and 2.4.18 are not defined for $\frac{1}{v^2} = p^2$ and this occurs for $z = z_{max}$, the turning point depth, we prefer to use the τ definition (2.4.19):

$$\tau = T - pX = \int \frac{\sqrt{\frac{1}{v^2} - p^2}}{v^2\left(\frac{1}{v^2} - p^2\right)} dz - \int \frac{p^2\sqrt{\frac{1}{v^2} - p^2}}{\frac{1}{v^2} - p^2} dz = \int \sqrt{\frac{1}{v^2} - p^2} dz \tag{2.4.20}$$

that we can decompose as:

$$T - pX = \int_{z_0}^{z_{max}} \sqrt{\frac{1}{v^2(z)} - p^2} dz + \int_{z_{max}}^{0} \sqrt{\frac{1}{v^2(z)} - p^2} dz \tag{2.4.21}$$

From equation 2.4.19, by deriving with respect to p, we obtain:

$$\frac{d\tau(p)}{dp} = -X(p) \tag{2.4.22}$$

and we can explore the values of p to find the one that minimizes the difference between real epicentral distances of receivers and the calculated ones: $|X_{obs} - X_{theo}|$.

For a fixed velocity model and given a source-receiver geometry, there is only one seismic ray that link them and so we can uniquely determine the parameter p. Considering more source-receiver couples and determining p for all of them, we construct our inverse problem with a cost function defined as

$$\Phi(\overline{m}) = \sum_{i=1}^{N} \frac{1}{N} \left(T_{obs_i} - T_{theo_i}\right)^2 \tag{2.4.23}$$

where T_{obs} are the travel times measured from data and T_{theo} are calculated by eq. 2.4.21 fixing $X = X_{theo}$. The sum is taken over all N source receiver pairs. The vector $\overline{m}$ represents the velocity model parameters. As we make the assumption that velocity is a continuous function, a possible representation is through fixing the position of a certain number of nodes along depth and interpolate them by linear or spline functions. With this representation, the vector $\overline{m}$ consists of the values assumed by velocity in the fixed nodes.

The exploration for velocity distribution parameters is done using the downhill SIMPLEX method. The method uses the concept of a *simplex*, which is a special polytope of $N + 1$ vertices in N dimensions. Examples of simplices include a line segment on a line, a triangle on a plane, a tetrahedron in three-dimensional space and so forth.

For multidimensional minimization, we have to give our algorithm a starting guess, that is, an N-vector of independent variables as the first point to try. The algorithm is then supposed to make its own way downhill through the unimaginable complexity of an N-dimensional topography, until it encounters a (local, at least) minimum. Algorithm must be started not just with a single point, but with $N+1$ points (i.e. models), defining an initial simplex. Generally, once chosen your initial starting point $\mathbf{P}_0$, you can take the other N points as

$$\mathbf{P}_i = \mathbf{P}_0 + \delta_i \mathbf{e}_i \tag{2.4.24}$$

where the $\mathbf{e}_i$'s are N unit vectors, and δ_i are the increments for each vector direction. Since this method is based on local exploration of the parameter space, we decided to make it more "global". To do that, the initial points are chosen not by increasing $\mathbf{P_0}$ in each direction, but generating $N+1$ random points chosen in the neighborhood of $\mathbf{P_0}$.

The downhill simplex method now takes a series of steps, most of them consist in just moving the point where the cost function is largest ("highest point") through the opposite face of the simplex to a lower point. These steps are called reflections, and they are constructed to conserve the volume of the simplex. When it can do so, the method expands the simplex in one or another direction to take larger steps. When it reaches a "valley floor", it contracts itself in the transverse direction and tries to move down the valley. In Figure 2.4.2 are shown examples of these typical steps for a tridimensional parameter space. It is possible to terminate the procedure when the vector distance moved in that step is fractionally smaller in magnitude than some tolerance *tol*. Alternatively, we could require that the decrease in the cost function value in the terminating step is fractionally smaller than some tolerance *ftol*. At the same time we require that the cost function becames smaller than a threshold *cmin*.

2.4.3 Test and results

As a first test for this method, synthetic travel times were generated for a smooth continuous velocity model. This "true" velocity model was constructed with a cubic spline with seven nodes equally spaced in a range of depth from 0 to 6 km. To add complexity, we decided to not let velocities just increasing with depth adding a low velocity zone from $z_1 = 2km$ to $z_2 = 4km$. The source-receiver geometry is shown in Figure 2.4.3 and consists of 20 sources and 20 receivers placed in a way to maximize the sampled space by ray paths. To compute synthetic travel times we implemented a ray tracing algotithm which "draws" the seismic rays that link each source with each receiver (Figure 2.4.3). The starting simplex was build considering 8 different models which nodes are randomly chosen between $1km/s$ and $9km/s$. In Figure 2.4.4 are shown all the initial models together with the true model and the final one obtained by the inversion. It is clear that results in quite good and the method is able to recover the original model used to generate travel times, also starting from velocity

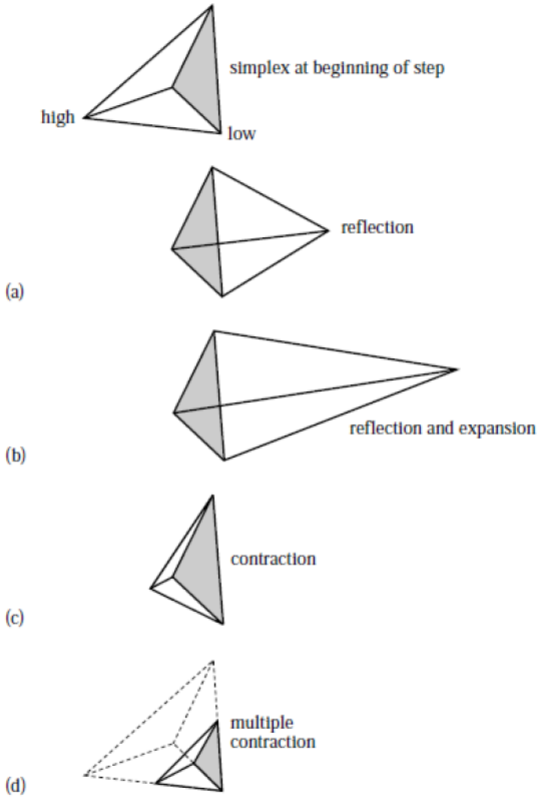
simplex at beginning of step
high
low
reflection
(a)
reflection and expansion
(b)
contraction
(c)
multiple
contraction
(d)

Figure 2.4.2: Possible outcomes for a step in the downhill simplex method. The simplex at the beginning of the step, here a tetrahedron, is shown, top. The simplex at the end of the step can be any one of (a) a reflection away from the high point, (b) a reflection and expansion away from the high point, (c) a contraction along one dimension from the high point, or (d) a contraction along all dimensions towards the low point. An appropriate sequence of such stepswill always converge to a minimum of the function. (Numerical Recipes, 1992)

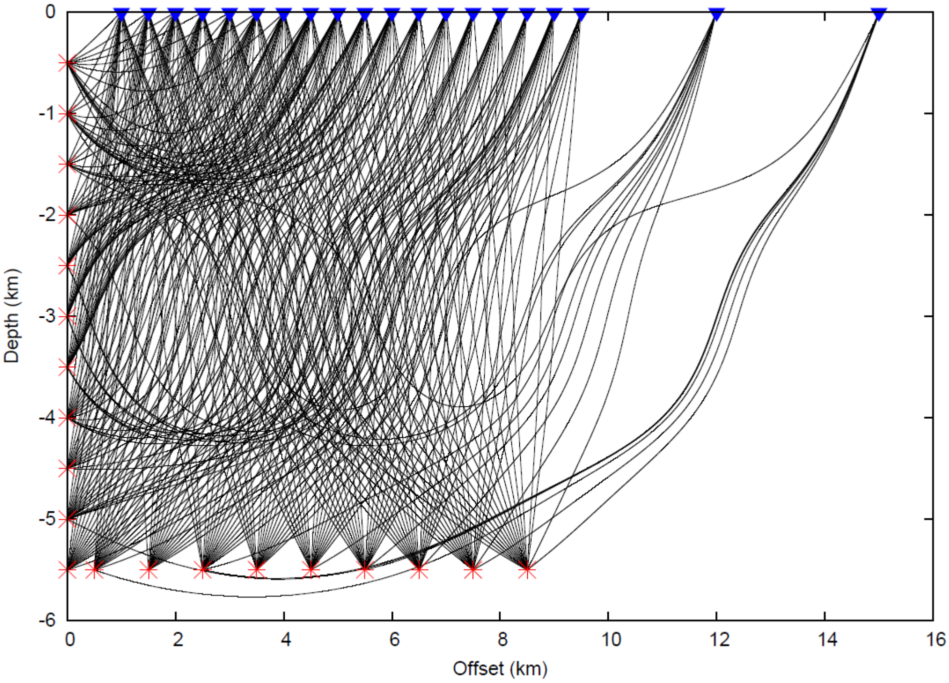

Figure 2.4.3: Sources (red stars) and receivers (blue triangles) positions and ray paths considered in the synthetic test.

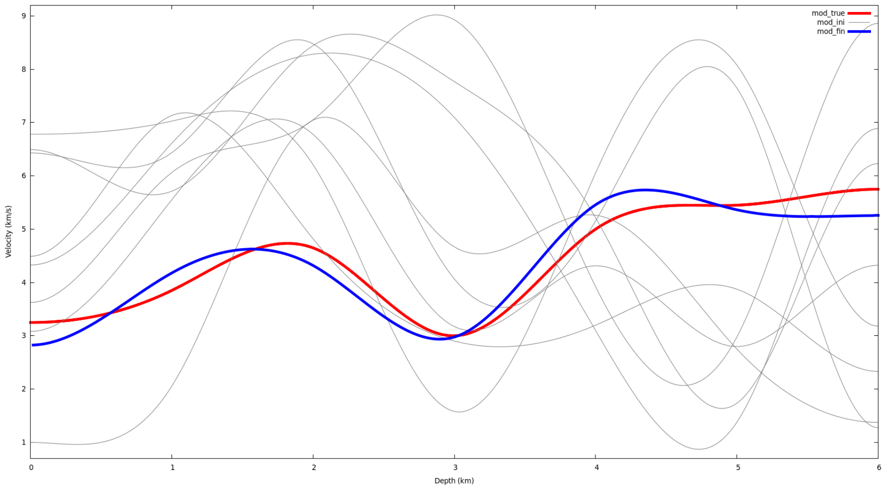

Figure 2.4.4: Velocity distribution versus depth for the starting models defining the initial simplex (grey lines), the "true" model (red line) and the final one obtained from the inversion (blue line).

distributions that are far away from the real one. After this synthetic test, we decided to apply the method to a real case study. Since travel time measures are really sensitive to earthquake locations, to be sure of non introducing systematic uncertainties, to perform this test we considered data provided by the extended marine active seismic survay (SERAPIS) carried out in the bays of Naples and Pozzuoli in September 2001. SERAPIS had the aim of investigating shallow structure and detecting the deeper magmatic system of the submerged part of the caldera using seismic tomography and migration techniques (Zollo et al., 2003; Judenherc and Zollo, 2004). Starting from a total database of traces from 75000 three-component records acquired by 30 seabottom receivers (OBS), we selected one of this receiver placed in the middle of Pozzuoli bay from which we extracted 2000 first P arrival times (Figure 2.4.5). A data selection was made to esclude travel times that are far from the the dromochrone trend and probably due to 2D or 3D complexity of the propagation medium (Figure 2.4.6). Average 1D P-velocity model proposed in previous study (Zollo et al., 2008) based on PP and PS travel times, and on PS-to-PP amplitude ratios was used as reference model to compare with our results (Figure 2.4.7). All velocity

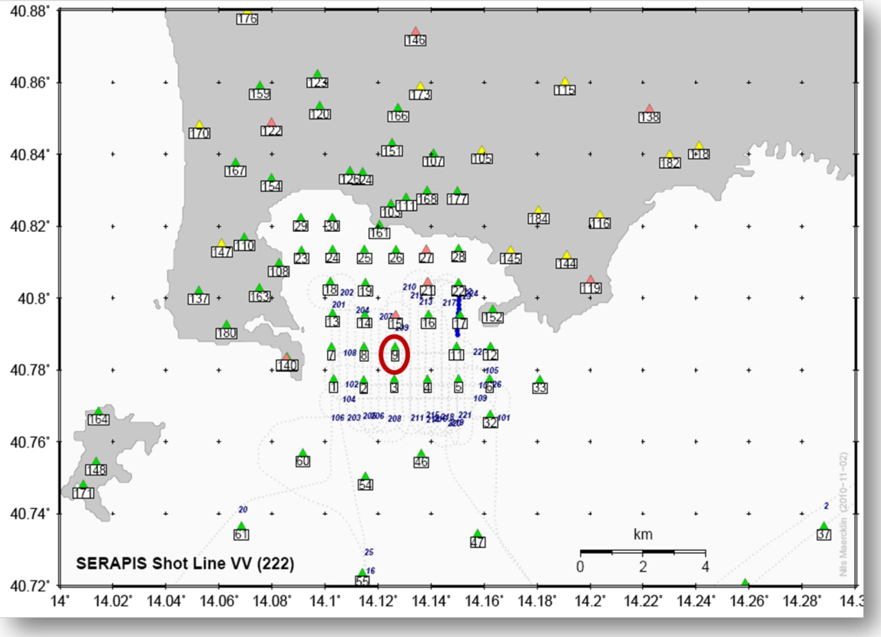
SERAPIS Shot Line VV (222)
km
0
2
4
40.88°
40.86°
40.84°
40.82°
40.8°
40.78°
40.76°
40.74°
40.72°
14°
14.02°
14.04°
14.06°
14.08°
14.1°
14.12°
14.14°
14.16°
14.18°
14.2°
14.22°
14.24°
14.26°
14.28°
Nils Maercklin (2010-11-02)

Figure 2.4.5: Map of the SERAPIS survay: airgun shots (grey dots), seismic stations and seabottom receivers (triangles). Considered station is circled in red.

models were parametrized by 8 control nodes at fixed depths (from $0km$ to $10km$) interpolated by a cubic spline. Starting models to construct the initial simplex were obtained choosing randomly the velocity values for each node in a range delimited by the two gradiend:

$$\begin{aligned} v_{min}(z) &= 0.35z + 0.5 \\ v_{max}(z) &= 0.75z + 2.5 \end{aligned}$$

In Figure 2.4.8 are plotted the initial models and the best model obtained from the inversion. Comparison between 1D model proposed by Zollo et al. (2008) is also shown to highlight the quite good agreement with results obtained with a completely different approach. Nevertheless, looking at the final model, it is possible to note a typical phenomenon related to polynomial and spline interpolation, such as artificial oscillation between two control points. In polynomial interpolations, we refer to as Runge's phenomenon. Since spline are particular curves that is piecewise-defined, and possesses a high degree of smoothness at the places where the polynomial pieces connect, Runge's phenomena are much less evident. However, when we have two near control nodes with very similar value of the function, the curve will have an oscillation between them. This is the case relative of what we observe in the final velocity model between 1 and 3 km depth. To avoid this numerical effect, we have planned to use different kind of interpolations, e.g. the linear interpolation should be better. Another possibility is to introduce in our misfit function a parameter of penalization to constrain the procedure to discard models with non realistic numerica artifact, or a smoothing operator to eliminate polynomial oscillations.

Another aspect to highlight in our results is related to the deepest velocity inversion in our final model which reasonably could correspond to the low velocity layer retrieved by Zollo et al. (2008). What makes this method interesting is related to the opportunity of obtaining smooth continuous velocity distribution with depth which, generally, are required as starting point for a 2D-3D tomographyc inversion. By these two simple applications, it results clear that this kind of approach could be used to rapidly obtain information about the propagation media in geologically complex areas for which a complete 3D wavefield representation should be planned. The use of interpolating functions like cubic spline makes possible to recover a smoothed version of medium discontinuity which can be very useful for reconstructing 3D complex structures.

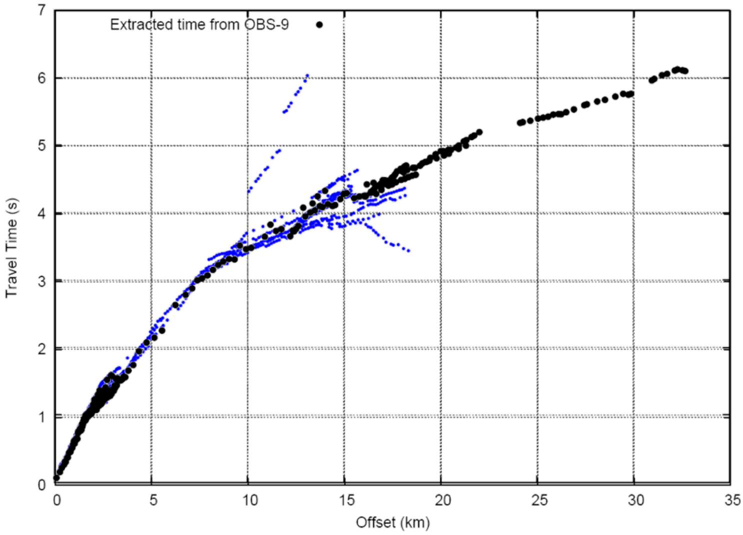

Figure 2.4.6: Selected 272 travel times used for the inversion procedure (black dots) versus distance from OBS-9. Blue dots are relative to all 2000 first P arrival times measured on traces recorded by this receiver.

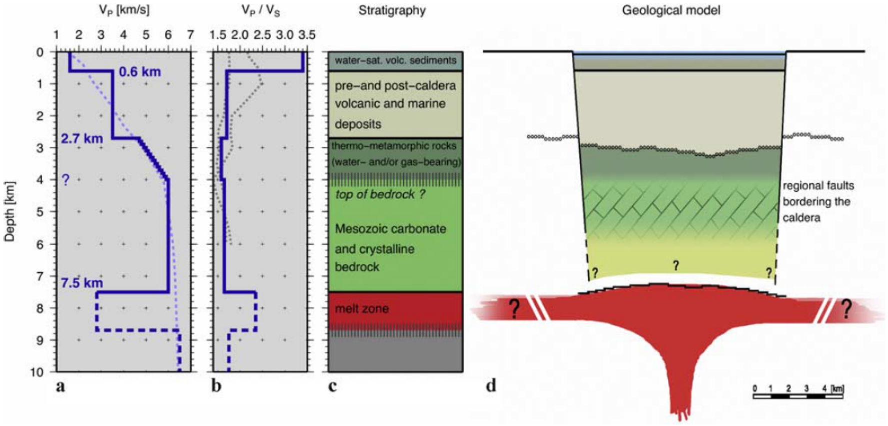

Figure 2.4.7: Geophysical and structural model of the deep structure of the Campi Flegrei caldera. (a) Average 1-D P-velocity model for the Campi Flegrei caldera, based on PP and PS travel times, and on PS-to-PP amplitude ratios. The dashed line is the average of the 3-D P-velocity model in the study area. (b) Vp/Vs ratio as a function of depth, as estimated in the present study. The dotted lines are two Vp/Vs depth profiles that were estimated from the local earthquake tomography (Vanorio et al., 2005). C: Stratigraphic model. D: Geological sketch model of the Campi Flegrei caldera. (from Zollo et al., 2008).

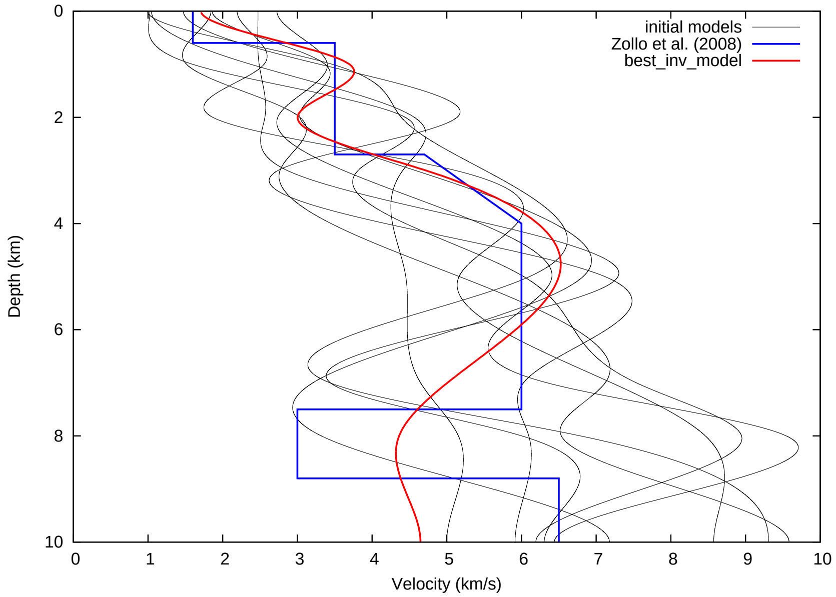

Figure 2.4.8: Initial models (interpolated by cubic splines) for starting simplex (gray line) and comparison between final best model (red line) and the one proposed by Zollo et al., 2008 for the Pozzuoli bay (blue line).

2.5 Empirical Green's functions

Numerical Green's functions are frequency limited because of the poor description of propagation effect at low wavelengths. This is due to the accuracy of both 1D and 3D tomographyc Earth's models, generally non sufficient to represent small scale heterogeneities. For this reason we are allowed to use numerical Green's functions to represent medium elastic response up to few Hz (generally 1-2 Hz).

To avoid this limit, under the hypothesis of linear wave propagation, the Green's functions may be replaced by the records of small earthquakes occurring on the same fault with the same focal mechanism and the same stress drop of the target event we are going to simulate. Commonly we refer to this small earthquakes as Empirical Green's functions (EGFs) (Irikura, 1983). For a large earthquake, a database of EGFs could be represented by the records of the aftershocks following the main event. The EGF behaves as a localized moment source which can replace the numerical Green's function in the representation integral (1.3.1), appropriately normalized by the seismic moment (Hutchings and Wu, 1990). Each EGF can be confused with the impulse response of the propagating medium at frequencies smaller than their relative corner frequency. Beyond this limit, the finite source effects of the small earthquakes start to appear in the data. To be sure that point source approximation is valid, we have to consider earthquakes with mgnitudes at least 2 point smaller than the target event.

Since the EGFs describe in an accurate way the propagation effects even at high frequencies, their use may broaden in principle the investigation band of the seismic source. However, several drawbacks limit the applicability of the EGFs and a special care needs to be taken when they are used for the simulation of strong motion records. Generally, accelerometric networks do not record the EGFs with the same accuracy of the mainshock, but the ambient noise very often pollutes the low-frequency band of the small event because of instrumental sensitivity and dynamic range. So that, making a selection from an aftershock database, we have also to ensure that their signal to noise ratio is sufficiently high to avoid artifact in synthetic data. To improve the quality of the aftershock records, strong motion stations should be, also, complemented with short or intermediate period sensors. A particular care should be devoted to the determination of the focal mechanism and the earthquake location, that are not an easy task for very small earthquakes (this gives the lower limit for the event selection magnitude range). Finally, EGFs distribution over the fault plane may not be uniform. Aftershocks are likely to occur on fault regions that have not slept during the mainshock rupture. In fault areas where the largest slip occurred, the stress level mostly dropped down to the dynamic value during the main rupture and the probability that the same patch slips again during an aftershock rupture is very low. As a consequence, the number of available EGFs is smaller than what required by the synthetic simulation and their location on the fault plane may not be optimal for retrieving the details of the main rupture. Hence, specific interpolation algorithms are needed to resample the EGFs on the fault plane and to compute the representation integral up to the frequencies of interest (Hutchings, 1994).

Chapter 3

A Case study: the 2009, L'Aquila earthquake

3.1 Introduction

On April 6 (01:32 UTC), 2009 a M_W 6.3 normal faulting earthquake struck the central area of the Abruzzo region in central Italy. The earthquake heavily damaged the city of L'Aquila and its surroundings, provoking 308 casualities, 70000 evacuees and incalculable losses to the artistic and cultural heritage. Almost 3000 events with $M_L \geq 1.9$ occurred in the area during 2009 that were registered and located (Chiaraluce et al., 2011a).

The L'Aquila mainshock ruptured a normal fault located in the extensional tectonic setting of central Apennines (Chiarabba et al. 2010; Chiaraluce et al. 2011a). Different studies have pointed out the complexity of the earthquake nucleation (Lucente et al. 2010), the initial stages of the rupture history (Ellsworth & Chiaraluce 2009; Di Stefano et al. 2011) and the subsequent coseismic rupture propagation (Cirella et al. 2009, Cirella et al. 2012).

3.2 Geological and seismotectonic context

The Central Appennines region in Italy, is characterized by a continental crust in an extensional stress regime, lying within the zone of convergence between the Eurasian and African plates. The current rate of extension is $2-3\,mm/year$

(Hunstad et al., 2003) and its orientation is consistent with available focal mechanism solutions (Montone et al., 2004) and geological data (Lavecchia et al., 1994). Extensional actions take place from W to E, leading to the opening of the Tyrrhenian sea and giving rise to the reactivation of the exiting normal structures and the creation of new normal fault systems. This activity produced large intermountain extensional basins such as L'Aquila, Sulmona and Fucino basins, filled by Plio-Quaternary continental sediments (Cavinato and De Cellis, 1999; Galadini and Galli, 2000). Since their formation, alluvial and lacustrine sediments were deposited in these basins, leaving the imprint of the different tectonic stages and climate changes that affected them. The L'Aquila basin is one of the most important of these intermountain basins in Central Italy. A compilation of the active faults, defined as geological structures that have an established record of activity in the late Quaternary (past $125\,Kyr$) and a proved or potential capability of generating major earthquakes ($M \geq 5.5$), of the Central Appennines was made by Boncio et. Al. (2004). Figure 3.2.1 displays surface projections of such active faults that are spread along three main alignments: the Eastern alignment extend from Mt. Vettore to Campotosto and Gran Sasso, the intermediate alignment extends from Gubbio to Gualdo Tadino, Cofiorito, Norcia, L'Aquila and Sulmona, and the Western alignment extends from Umbria valley to Rieti, Fucino and Barrea.

The L'Aquila basin is a tectonic depression of the Central Appennines, located between the Gran Sasso and the Monti d'Ocre Velino Sirente. The northern edge of the basin is bordered by the Monte Pettino fault, which is part of the $WNW-ESE$ segmented fault system with late Quaternary activity (Blumetti et al., 2002). The region exhibits characteristics similar to those observed in the Southern Appennines (e.g. Irpinia region), where the largest earthquakes are related to normal system striking along the chain direction. Moderate magnitude earthquakes ($4 \leq M \leq 6$) recorded instrumentally in the past 20 years, as well as large historical earthquakes with long recurrence intervals occur in this area, mainly concentrated in the upper crust, at depths $< 15\,km$ (Boncio et al., 2004). Field, geology-based studies revealed the location and geometry of major faults. Some of them are thought to be responsible for the larger historical earthquakes that occurred in the region, such as the Fucino fault system associated to the 1915 M_S 7 earthquake (Ward and Valensise, 1989). The closest and largest damaging historical earthquakes that struck the region occurred in 1461 close to the city of L'Aquila ($I_{max} = X$), and in 1703 slightly to the north ($I_{max} = XI$). Some authors (Atzori et al., 2009) suggested that the 1461 event may have occurred on the Paganica-San Demetrio segment which is responsible also for the 2009 mainshock.

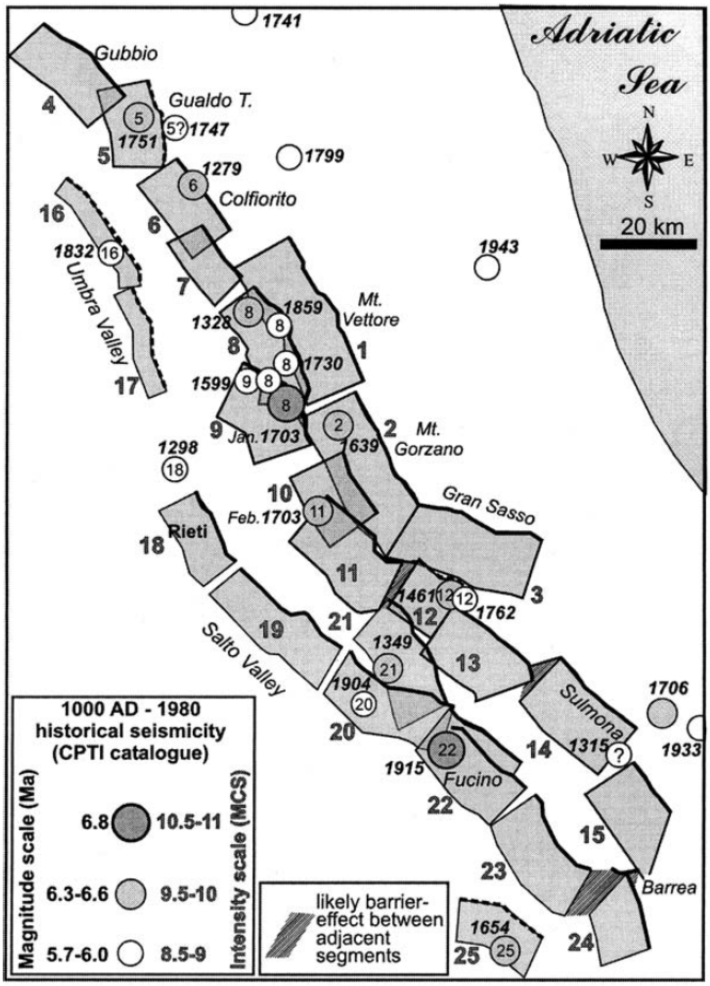
Adriatic Sea
N
W
E
S
20 km
1741
Gubbio
Gualdo T.
4
5
1751
5?
1747
1799
1279
6
Colfiorito
16
1832
Umbra Valley
17
7
1943
1328
8
1859
Mt. Vettore
1
1730
1599
9
Jan.1703
2
1639
Mt. Gorzano
1298
18
10
Feb.1703
11
Gran Sasso
Rieti
3
1461
12
1762
19
21
1349
13
Salto Valley
1904
20
Sulmona
1706
1315
?
1933
14
22
1915
Fucino
15
23
Barrea
1654
25
24
1000 AD - 1980 historical seismicity (CPTI catalogue)
Magnitude scale (Ma)
Intensity scale (MCS)
6.8
10.5-11
6.3-6.6
9.5-10
5.7-6.0
8.5-9
likely barrier-effect between adjacent segments

Figure 3.2.1: Map of the seismogenic areas for the Umbria-Marche-Abruzzo Apennines and epicentres of historical earthquakes larger than $VIII$ on the MCS scale ($M \geq 5.7$) from C.P.T.I. catalogue (Working Group CPTI, 1999); dates refer to the year of earthquake occurrence (from Boncio et al., 2004).

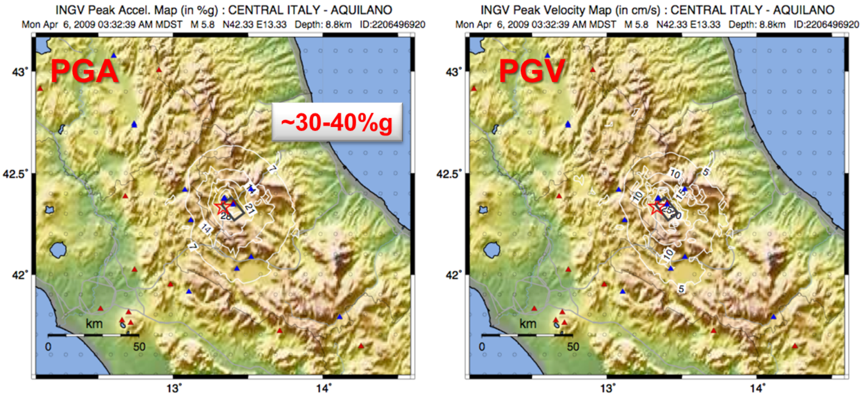
INGV Peak Accel. Map (in %g) : CENTRAL ITALY - AQUILANO
Mon Apr 6, 2009 03:32:39 AM MDST M 5.8 N42.33 E13.33 Depth: 8.8km ID:2206496920
PGA
~30-40%g
INGV Peak Velocity Map (in cm/s) : CENTRAL ITALY - AQUILANO
Mon Apr 6, 2009 03:32:39 AM MDST M 5.8 N42.33 E13.33 Depth: 8.8km ID:2206496920
PGV
43˚
42.5˚
42˚
13˚
14˚
km
0
50

Figure 3.3.1: PGA and PGV shakemaps computed by INGV few days after the main event using all available data.

3.3 Strong motion data: mainshock and aftershock analysis

The strong motion data recorded during the earthquake in the near-fault region exhibit large amplitudes, localized peaks and a strong space variability, this latter being also observed in pattern of the damage distribution. Figure 3.3.1 shows PGA and PGV maps computed by INGV few days after the event using all data relative to the mainshock. As it is possible to see, ground acceleration reaches peak values of $\sim 30\% - 40\%$ of g near L'Aquila city.

The mainshock, located at around $9\,km$ depth beneath the town of L'Aquila, activated a $\sim 50°$ SW-dipping and $\sim 135°$ NW-trending normal fault with a length of about $15 - 20\,km$. The aftershocks sequence activated a region of $10\,km$ of the upper crust up to the surface. The geometry of the fault is coherent with the mapped San Demetrio-Paganica and Mt. Stabiata normal faults. The mainshock fault plane was activated by a foreshock sequence that culminated with a M_W 4 on March 30 (13:38 UTC). There is a second major structure, located to the north close to Campotosto and controlled by a M_W 5 event, which occurred on the same day of the mainshock (April 6 at 23:15 UTC), and by a M_W 5.2 event occurred few days later (April 9 at 00:53 UTC).

This earthquake hence represents an interesting case test to investigate near-fault effects and to understand the role played by the source and the large scale wave propagation on the observed ground motion and ground motion variability. Moreover, beyond the main event, records of aftershocks and foreshocks form a database of Empirical Green's functions (EGFs) that can be used as the impulse response of the medium in the ground motion simulation. Specifically, records at the accelerometric network allow for calibration of source parameters by comparison with real observations, whilst records at the temporary network allow an estimation of the ground motion in sites where no data from the main event are available.

3.4 Numerical Green's functions for L'Aquila region

To perfom synthetic simulations, we computed the Green's tractions for each station and each frequency, after definition of the , velocity and density models, and the focal mechanism. The Green's tractions are computed by using the discrete wavenumber integration technique (Bouchon, 1981; Coutant, 1989). This technique assumes that the Earth structure is a 1D layered medium and provides the complete wave field, so that all P and S waves, surface waves, and near-field terms are included in the synthetic seismograms. Moreover, this method allows for the modeling of the anelastic attenuation.

Green's tractions are used to model the medium response at low frequency, in particular we have considered the range $[0.05; 0.7]$ Hz. As 1D crustal velocity model we chose the one proposed by Bianchi et al. (2010) based on receiver function analyses. We adopt the model derived at the FAGN station (National Seismic Network), which is localized close to the southeastern termination of the fault, because in previous study it is found to be more appropriate to represent the general wave propagation over the whole study area (Ameri et al., 2012). The model was semplified by removing the velocity inversion between $13\,km$ and $19\,km$ (see Table 3.1).

3.5 Empirical Green's functions: selection and analysis

The large number of aftershocks and foreshocks of the 2009 L'Aquila earthquake allowed us to get a potential catalog of waveforms hat can be used as the impulse response of the medium in the ground motion simulation. Starting from the

Depth (km)	$V_P\,(km/s)$	$V_S\ (km/s)$	$\rho\,(g/cm^3)$	Q_P	Q_S
0	3.16	1.70	2.50	200	100
1	4.83	2.60	2.84	400	200
2	5.76	3.10	2.94	400	200
5	6.51	3.50	3.15	400	200
27	7.00	3.80	3.26	600	300
42	7.80	4.20	3.50	800	400

Table 3.1: Model based on Bianchi et al. (2010) V_S profile for station FAGN. V_P values are computed adopting a $V_P/V_S = 1.86$ (Ameri et al., 2012).

whole aftershocks database, we have selected around 400 events recorded in the first month after the mainshock, The first selection criterion is related to the signal to noise ratio in a specific frequency range (from 0.2 Hz to 20 Hz), that was chosen to be larger than 3 in all the frequency range. Then, considering the locations obtained by Chiaraluce et al. (2011), we have selected those of them located almost on the same plane of the main event. Moreover, we know that their corner frequency must be sufficiently larger than the one of the main event, indicating that we considered those events with magnitudes at least $2-3$ point smaller than the magnitude of the mainshock. For the computation of the corner frequencies and the verification of constant stress drop hypothesis (according to the self-similarity assumption used for the discretization of the fault described in the previous section), a two-step inversion of displacement spectra was performed to jointly extract the quality factor Q and the source parameters. Results of these analysis are shown in Figure 3.5.1.

Respecting all these criteria, we selected 10 aftershocks with local magnitude between 3.5 and 3.7 (the magnitude range is small to choose the EGFs as similar as possible). At the end, we have to check also if the focal mechanisms of the EGFs are almost the same of the target event. For 9 of these 10 events the focal mechanisms are available from Scognamiglio et al. (2010) and shown in Table 3.2 (Figure 3.5.2). Considering 9 stations from the National Accelerometric Network (Department of Civil Protection), 2 from the INGV national network, 1 from the MedNet (Mediterranean Seismic Network), 2 stations from the INGV mobile network and 2 stations from the mobile network of the LGIT of Grenoble, we selected 16 stations at different azimuths and distances from the fault plane. computed displacement spectra of the EGFs for each station (not all the stations recorded all the EGFs, depending on the distance,but we still have, for the worst cases, at least 3 stations recrding a single EGF), scaled them

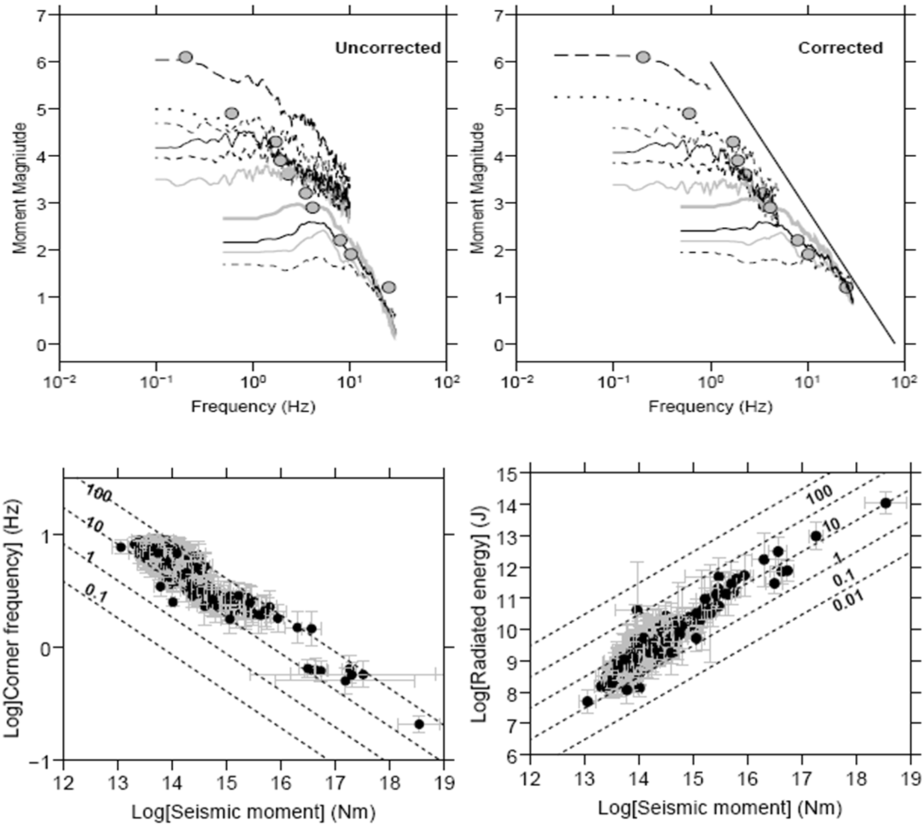

Figure 3.5.1: Earthquake self-similarity: we observe a constant stress-drop scaling of source parameters.

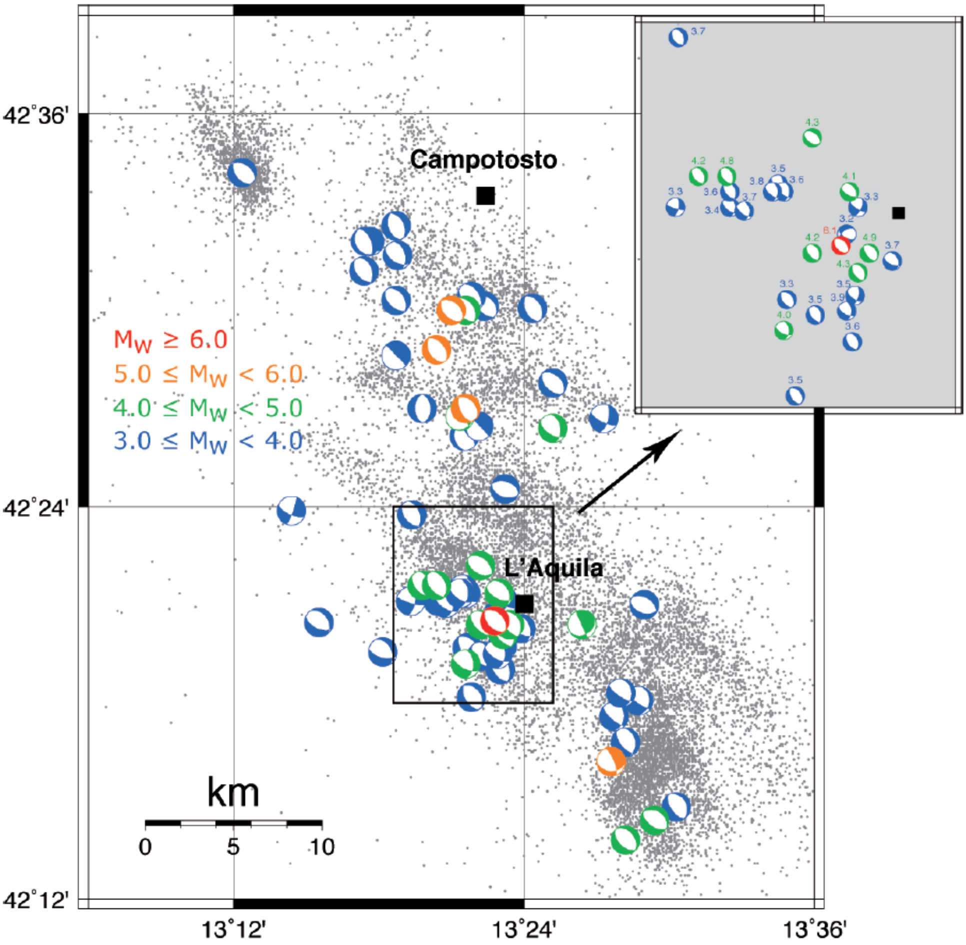
42°36'
Campotosto
$M_W \geq 6.0$
$5.0 \leq M_W < 6.0$
$4.0 \leq M_W < 5.0$
$3.0 \leq M_W < 4.0$
42°24'
L'Aquila
km
0
5
10
42°12'
13°12'
13°24'
13°36'

Figure 3.5.2: Map of the L'Aquila 2009 seismic sequence. Epicenters (from 2008/12/01 to 2009/11/30) are shown using gray dots. The focal mechanisms determined using the TDMT technique are shown as beach balls with different colors depending on M_W. The mainshock mechanism is in red. (From Scognamiglio et al., 2010).

Date - Time	M_L	M_W	Strike	Dip	Rake
2009.04.06.01.32.40	5.9	6.3	133	54	-102
2009.04.06.04.47.54	3.6	3.8	129	59	-123
2009.04.06.10.36.18	3.5				
2009.04.06.22.47.14	3.7	3.6	104	58	-120
2009.04.08.03.00.35	3.6	3.6	131	73	-155
2009.04.08.11.35.57	3.5	3.3	107	79	-152
2009.04.10.15.46.18	3.5	3.2	120	60	-44
2009.04.12.09.48.59	3.5	3.3	122	74	-150
2009.04.13.19.17.58	3.5	3.4	130	61	-120
2009.04.21.15.44.36	3.7	3.5	139	54	-107
2009.04.30.13.01.01	3.5	3.5	131	60	-128

Table 3.2: Magnitudes and focal mechanisms for the mainshock and the 10 selected aftershocks

to an average seismic moment and corrected for a reference distance from the fault (hypocentral distance of the target event). We than calculated the mean and the standard deviation of these spectra and plotted the average standard deviation versus distance to point out the natural variability of the EGF at each station. It is possible to observe a decreasing trend with distance: at large distances the source-station path became almost the same for all the EGF so they look similar. Also there is a large variability of sigma for stations that are almost at same distances (see Figure 3.5.3). Due to this natural variability of the spectra, the choice of a particular EGF produces an epistemic uncertainty in the simulations that is evaluated and shown in the next sections.

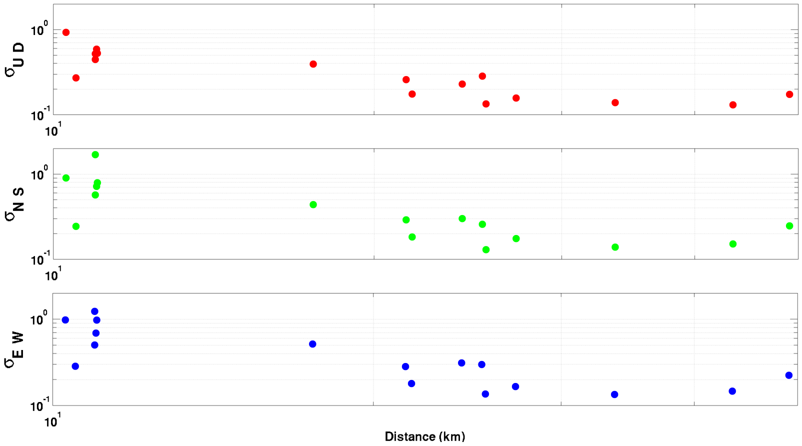

Figure 3.5.3: Distribution of sigma versus distance for different stations.

Chapter 4

Source inversion of L'Aquila earthquake

4.1 Introduction

Using the methodology illustrated in the first chapter, we are going to present the results of a kinematic inversion of the L'Aquila earthquake. This event is an interesting case test because the large number of studies performed by several authors in the last years and the several source kinematic models obtained with different techniques (e.g. Cirella et al., 2009; Atzori et al., 2009; Ameri et al., 2012) have pointed out the complexity of this particular rupture process. This has led us to apply our method to obtain as much information as possible about this earthquake source process.

4.2 Data selection

To perform the inversion, we have have considered strong motion data recorded all around the epicentral area, at different distances. We have selected 11 three-component digital accelerometers of the RAN Network and the AQU (MedNet) accelerogram from alla the avlaible stations at regional scale that have recorded the mainshock (Figure 4.2.1). They were integrated to obtain ground velocity time histories and bandpass filtered between 0.05 and 0.3 Hz with a two-pole and two-pass Butterworth filter. Locations of these 12 stations are reported in

Stat. Name	Lat. (°)	Lon. (°)	Epi. Dist. (km)
AQU	42.354	13.405	2.45
AQK	42.344	13.40	1
AQG	42.373	13.336	4
GSA	42.42	13.52	14
FMG	42.268	13.117	23
ANT	42.418	13.079	23
AVZ	42.027	13.426	34.9
MTR	42.524	13.244	22.4
LSS	42.558	12.969	39
CLN	42.085	13.521	31.6
ORC	41.953	13.642	49.3
SUL	42.089	13.934	56.4

Table 4.1: Listi of selected stations with thei geographycal location and epicentral distance.

Table 4.1 in terms of latitude, longitude and distance from the epicenter.

The total length of the synthetic data is $81.92\,s$, the frequency step is $0.0122\,Hz$, and so 25 frequencies are used in the inversion. The synthetic and real displacements are obtained from the synthetic and the real velocities by integration in the frequency domain (Cotton et al., 1995).

4.3 Model parameterization

For the selected frequency range $[0.05-0.3]\,Hz$, the maximum resolvable wavelength on the fault plane is $5-10\,km$, corresponding to a Gaussian width of about $4\,km$. the dimension of the plane are $28\,km$ along the strike direction and $20\,km$ along the dip direction. We used a regular distribution of Gaussian functions along the strike and along the dip (the total number is: $N_g = 42$). The sample spacing in strike ($d\xi_1$) and dip ($d\xi_2$) direction is $500\,m$. According to Emolo (2001), we need an additional condition about the rise time τ:

$$t_{max} < \tau \tag{4.3.1}$$

where t_{max} is the maximum propagation time in a subfault and can be written as:

$$t_{max} = \frac{\sqrt{d\xi_1^2 + d\xi_1^2}}{v_r} \tag{4.3.2}$$

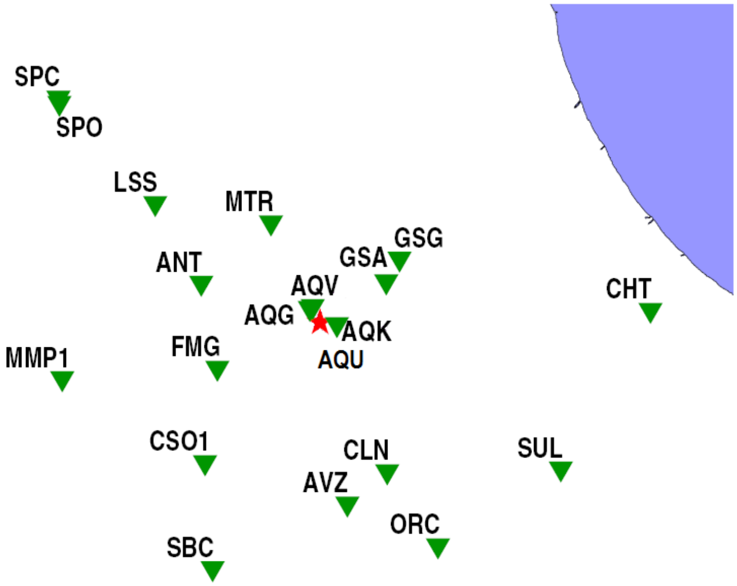
SPC
SPO
LSS
MTR
GSG
GSA
ANT
AQV
CHT
AQG
AQK
AQU
FMG
MMP1
CSO1
CLN
SUL
AVZ
ORC
SBC

Figure 4.2.1: Map of all the avalaible stations at regional scale which have recorded the mainshock.

Also considering a low value of rupture velocity $v_r = 2\,km/s$, since $d\xi_1 = d\xi_2 = 500\,m$, $t_{max} = 0.35\,s$. To respect the 4.3.2, we decided to use a rise time $\tau = 1\,s$, which is in general around the 10% (Heaton, 1990) of the total rupture time. For the rupture velocity we used $4x4$ control point grid, and we limited the variation range between 1.5 km/s and 3.5 km/s, while the slip velocity source time function is a rectangle (eq. 1.4.2).

4.4 Constant rupture velocity inversion

As fisrt stage, we started inverting only for the final slip distribution, fixing a constant value of rupture velocity v_r over the fault. Increasing linearly the rupture velocity in the range $[1.5 - 3.7]$ km/s bt step of $0.1\,km/s$, we compute the misfit function (eq. 1.5.6) between real and synthetic data for each model obtained. In Figure 4.4.1 is shown the value of the misfit as function of v_r. The lowest values of the misfit is reached for the highest values of v_r, in particular the minimum is for $v_r = 3.5\,km/s$. In Figure 4.4.2 we show the slip map obtained with this fixed value of v_r. Highest values of slip ($\sim 50\,cm$) are localized in a large patch in the deepest part of the fault (between 5 and $10\,km$ from the hypocenter) with a linear dimension of about $5\,km$, and in a smaller one close to the surface (around $15\,km$ from the hypocenter) with a linear dimension of about $1\,km$. There is also a quite significant amount of slip close to the nucleation zone. For all the inverted stations, we show also the comparison between real and synthetic data in terms of ground displacement for the considered frequency range (Figure 4.4.3). What we observe is that for the very near source stations (AQU, AQK and AQG), we are not able to reproduce real amplitudes especially for the horizontal components. Nevertheless, vertical component are quite well reproduced at these stations, except AQU for which synthetic and real waveform are similar but scaled in amplitude by a factor of 2. For GSA station there is also a good agreement, at least for the first part of the signals. If we look a bit far away from the epicentral area, we have not a good fit for all the inverted signals, except for CLN which is located south of the fault and probably is interested by directivity effects that here seem to be well reproduced.

4.5 Variable rupture velocity inversion

After this preliminary analysis, we made a complete inversion to retrieve both a slip and a rupture velocity distribution over the fault plane. We let v_r to vary

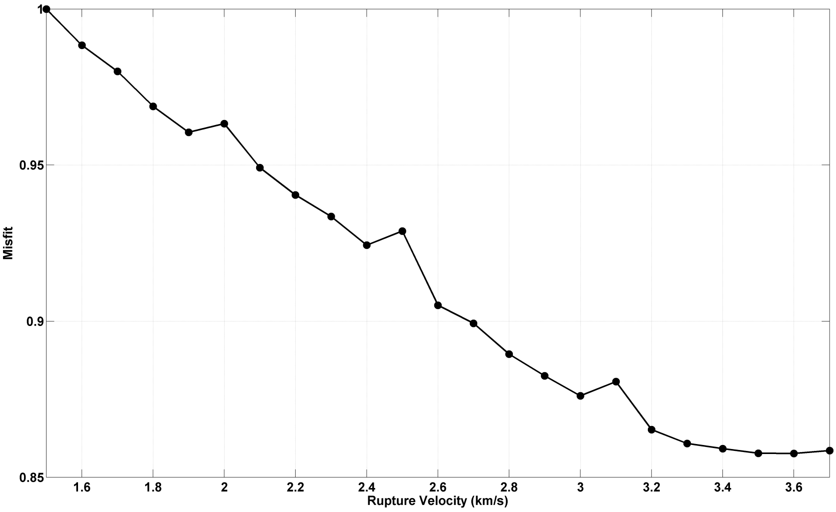

Figure 4.4.1: The figure shows the normalized misfit between real and synthetic data as function of the rupture velocity.

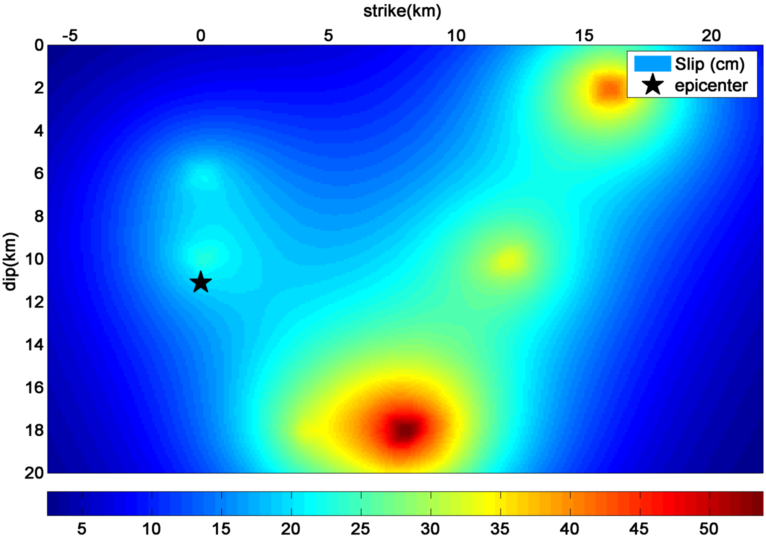

Figure 4.4.2: Final slip distribution obtained by inversion for a constant rupture velocity, $v_r = 3.5\,km/s$.

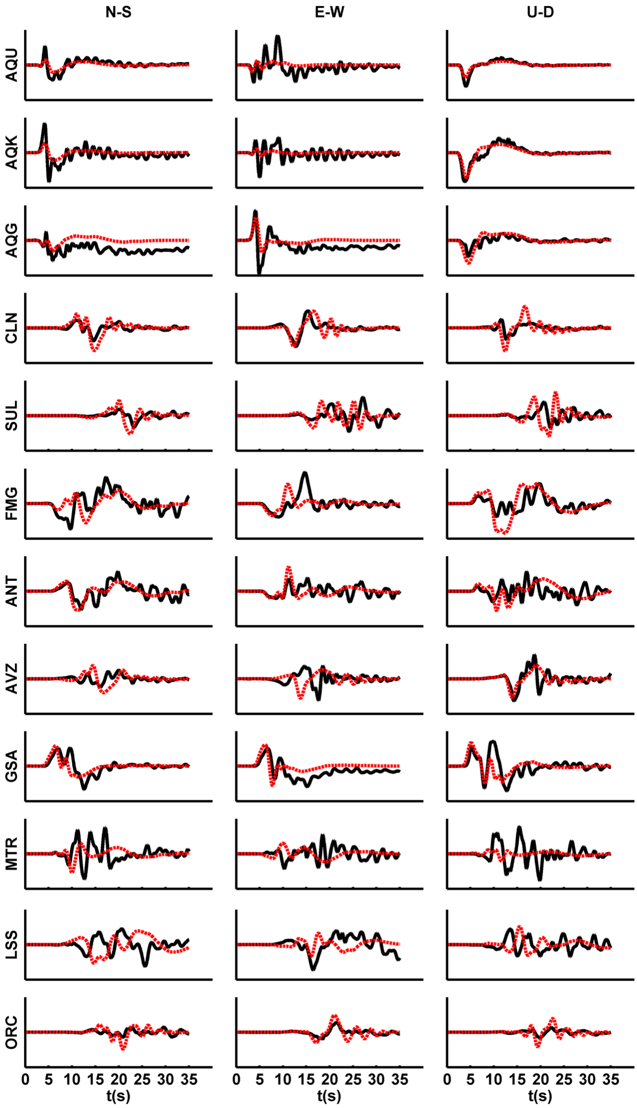

Figure 4.4.3: Synthetic ground displacement (red dashed lines) compared with real ones (black lines) for all the inverted stations. Data are shown in the frequency range used for the inversion: $0.05 - 0.3\,Hz$.

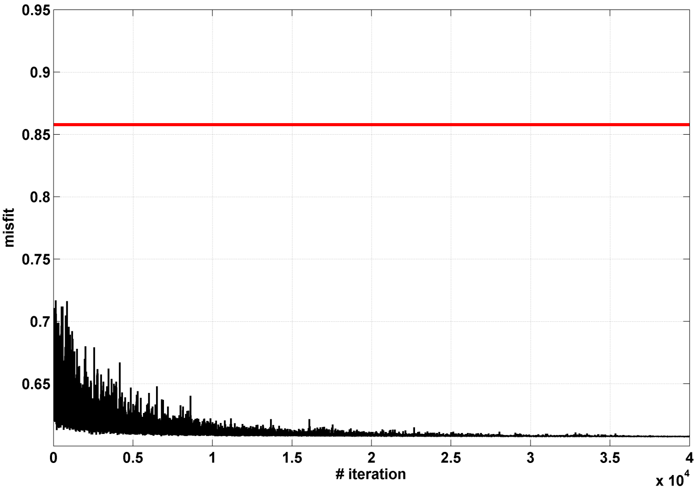

Figure 4.5.1: Smallest misfit per iteration between synthetics and observations as a function of number of iterations. Red line indicates the minimum value obtained for a constant rupture velocity ($v_r = 3.5\,km/s$).

between $1.5\,km/s$ and $3.5\,km/s$ considering results of the previous tests and the fact that our propagation model (Table 3.1) has a shear wave velocity of $3.5\,km/s$ between $5\,km$ and $27\,km$ and we wanted to respect the general assumption that $v_r < V_S$ (generally is $\simeq 0.8 - 0.9V_S$). With a variable rupture velocity, the misfit value is sensitively reduced, and so it means that the model is able to better reproduce observed ground motion for almost all the considered stations. We performed a total of 4×10^4 iterations in the inversion. In Figure 4.5.1 is shown the smallest misfit per iteration, normalized to the highest obtained value which is for a constant $v_r = 1.5\,km/s$ (see Figure 4.4.1). It demonstrate a relatively slow convergence, due to the strong nonlinearity of the problem, for the first 10^3 iterations and then an asymptotic trend around the minimum.

The best model obtained is quite different from the one shown in Figure 4.4.2. We find againg a large slip patch in the deepest part of the fault, but now here is concentrated large part of the total amount of slip and the respective value in the nucleation zone is reduced (Figure 4.5.2). From the rupture time isolines we can observe that there are two main propagation stage of the rupture:

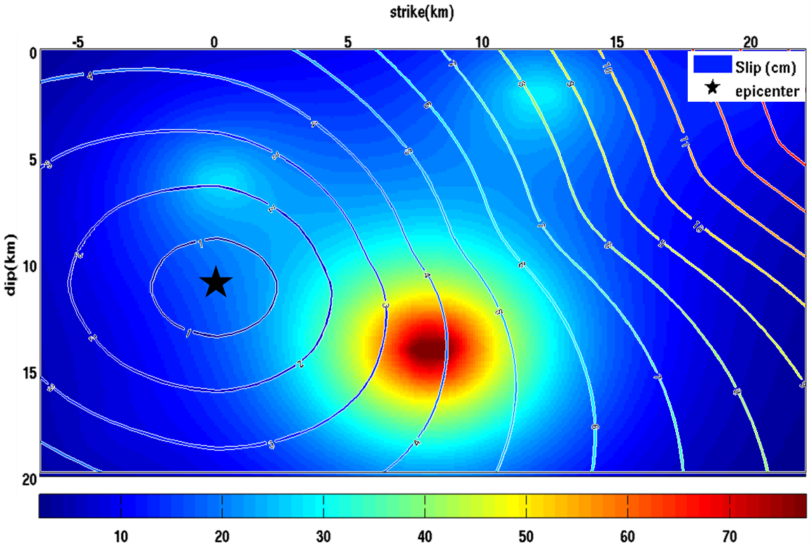

Figure 4.5.2: Best source model obtained from kinematic inversion in terms of slip distribustion (in color) and isolines of constant rupture time.

the first one is in the up-dip direction with an average velocity of 2.3 km/s; the second one is along strike with an average velocity of 2 km/s. If we look at the comparison between synthetic and observed data (Figure 4.5.3), we can see that there is a significant improvement in reproducing ground displacement. There are some reverberations That are not well reconstructed (e.g. the E-W component of AQU and AQK) maybe related to specific affect due to resonance of the L'Aquila basin. If this is the case, a more detailed 3D propagation model can be useful take into account these effects. It is important to note that the characteristic vertical pulse at L'Aquila stations (AQU,AQK and AQG) is well reproduced by this model, both in amplitude and shape.

To test our capability of resolving smaller wavelength over the fault surface, we tried to invert the same data in a larger frequency range: $0.05 - 0.7\,Hz$. The model obtained is shown in Figure 4.5.4 and effectively present an higher complexity in slip distribution and the propagation of the rupture is faster (average velocities along the two main direction are respectively 3 km/s and 3.3 km/s). Altought, if we compare the computed synthetics in this last model with

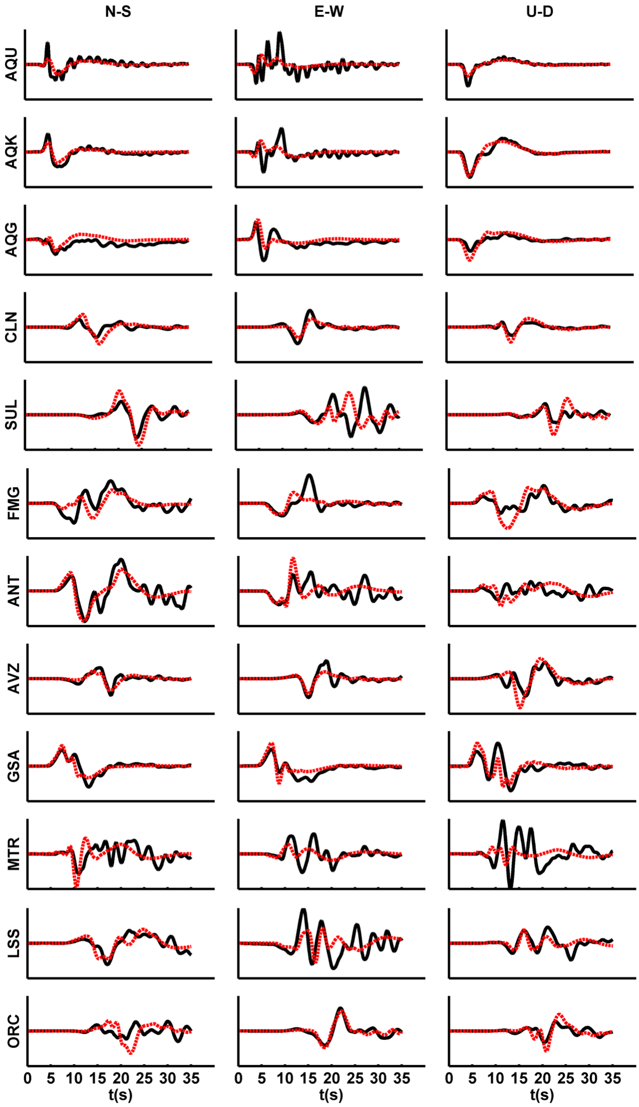

Figure 4.5.3: Synthetic ground displacement (red dashed lines) obtained with the model in Figure 4.5.2 compared with real ones (black lines) for all the inverted stations.

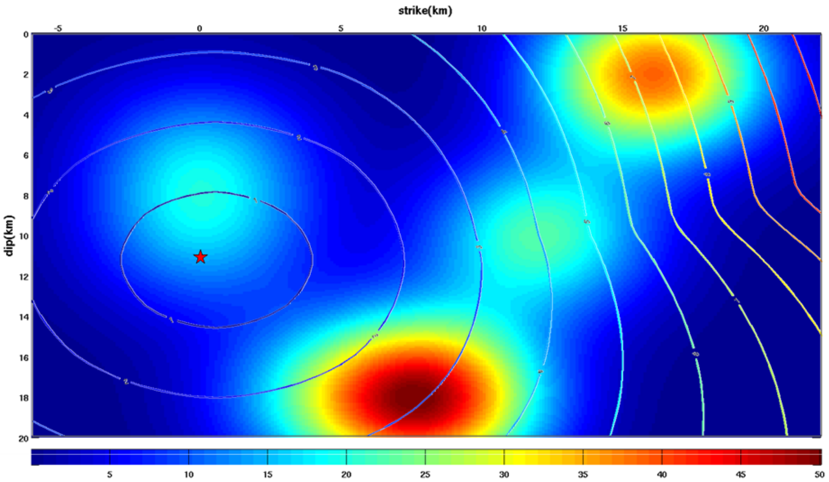

Figure 4.5.4: Slip map and rupture time isolines obtained from kinematic inversion with data selected in the frequency range $0.05 - 0.7\,Hz$.

real ones in this broader frequency range, they are not able to fit high frequency oscillations present in real records (Figure 4.5.5). It can be probably due to the incomplete propagation medium description at these frequencies because we are taking into account also 2D and 3D medium contribution in real data that are not modeled in synthetics. Also 1D crustal velocity models generally are not constructed to represent small medium heterogeneity. As an additional proof, we have compared the normalized misfit trend as funtion of number of iteration obtained for the two inversion in the two frequency range and it is clear that the values are significantly higher in the second one (Figure 4.5.6).

For all these reasons, we decided to adopt the second mode (Figure 4.5.2) as our low frequency reference model for all the analysis that we will present in the next sections.

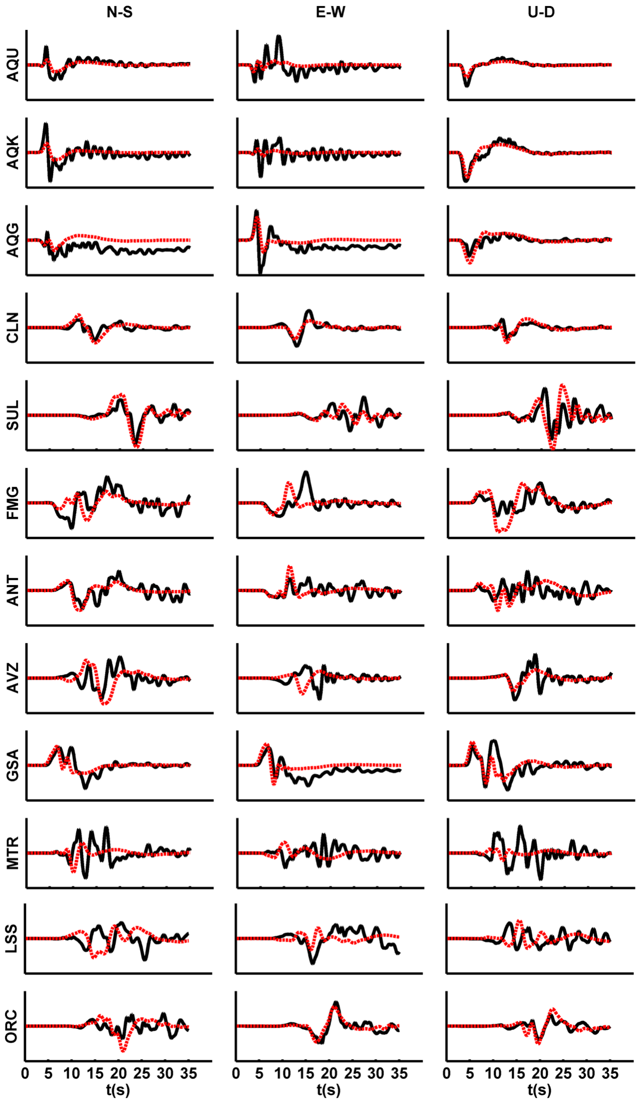

Figure 4.5.5: Synthetic ground displacement (red dashed lines) compared with real ones (black lines) for all the inverted stations. Data are shown in the frequency range used for the inversion: $0.05 - 0.7\,Hz$.

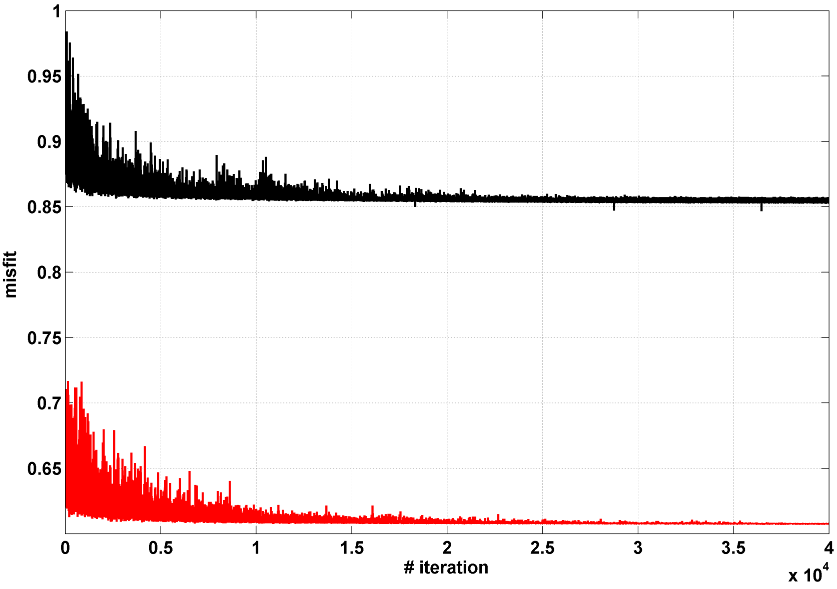

Figure 4.5.6: Comparison between misfit values versus number of iteration for two inversions made considering two different frequency range: $0.05 - 0.3\,Hz$ (in red) and $0.05 - 0.7\,Hz$ (in black).

Chapter 5

Broadband simulations

5.1 Introduction

Ground motion simulations have a considerable interest in seismology because they require our best knowledge on source process and propagation effect to obtain realistic and reasonable results. We have performed several broadband simulations of the 2009 L'Aquila earthquake combining low frequency signals, obtained with numerical technique, with high frequency simulations made using EGFs. After that we included a k^{-2} slip distribution to model high frequency source contributions. We used an opportune matching filter to couple the two simulations in the frequency domain and obtain broadband signals (Figure 5.1.1). The influence of the low frequency kinematic model obtained from the inversion is also investigated as well as the influence of the EGF selection.

5.2 Broadband simulation results

We computed broadband signals coupling numerical low frequency simulations showed in section 4.5 with high frequency simulations with empirical Green's functions summation. To compute high frequency synthetic records we solved the representation integral (eq. 1.3.1) in a discretized form. The source term is constructed supposing slip an v_r distribution obtained by kinematic inversion an assuming a triangle slip velocity function. For each subfault, this source term is convoluted with the EGF associated to that subfault (the nearest one) and than, the contribution of each of them is summed up with a proper time shift

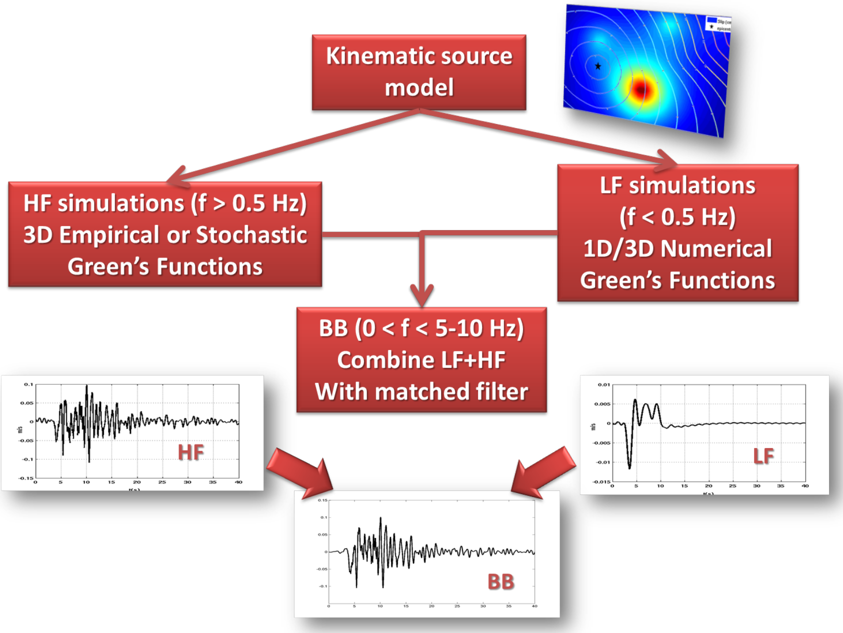
Kinematic source model
HF simulations (f > 0.5 Hz)
3D Empirical or Stochastic
Green's Functions
LF simulations
(f < 0.5 Hz)
1D/3D Numerical
Green's Functions
BB (0 < f < 5-10 Hz)
Combine LF+HF
With matched filter
HF
LF
BB

Figure 5.1.1: Schematic representation of the method used for coupling low and high frequency simulations.

depending on the rupture time. The selected frequency range of overlapping is $0.3 - 0.7\ Hz$.

Here we represented the simulated velocity amplitude spectra compared with real ones for three stations: AQU and AQG, which are in near source conditions, and CLN, which is a bit far from the epicentral area (Figures 5.2.1, 5.2.2 and 5.2.3). Triangle slip velocity function in frequency domain is defined by eq. 1.4.3 and has the typycal shape of a sinc functions represented in Figure 1.4.1. At high frequency its spectrum presents periodical "zeros" in corrispondence of frequencies proportional to half of the triangle width. Because of triangle width is exactly the rise time τ_r, if we set $\tau_r = 1\,s$, the first "zero" will be exactly at $2\ Hz$. This effect produces a significant amplitude decrease in high frequency simulations (green line in Figures 5.2.1, 5.2.2 and 5.2.3). To eliminate this problem we have generated a random rise time distribution over the fault with values chosen between $0.1s$ and $1s$ (red line in Figures 5.2.1, 5.2.2 and 5.2.3).
Comparison with real data shows a good agreement up to $0.5\,Hz$ for all the considered stations. At high frequency, the choice of random rise time produces an improvement for AQU and AQG and completely remove the spectrum decay for CLN station for which real data is retrieved for all the frequency range.

5.3 Broadband simulations with K^{-2} model

To describe properly the source contribution up to high frequencies we decide to adopt a K^{-2} model, in particular using the technique showed in section 1.6. Starting from the low frequency model obtained by kinematic inversion (Figure 4.5.2) we completed the slip spectrum in wavenumber domain following a K^{-2} decay. New slip distribution is showed in Figure 5.3.1.

We have done broadband simulations for several stations at different distances and azimuths with respect to the fault. Here we show results for five of them (AQU, AQK, AQG, GSA and FMG) in terms of acceleration waveform, Fourier amplitude spectra and response spectra (Figure from 5.3.2 to 5.3.6). Comparison with real observation is also shown. In general, for all the stations, we reproduce quite well the high frequency part of the signals (between 5 and 10 Hz) and the low frequency part that we have inverted. In the range between 0.5 and 5 Hz, real data have the highest amplitude and synthetic records are non able to fit them. This may depend probably on an incoplete or not adequate description of the source which is obtained by data only up to 0.3 Hz and then completed stochastically. To improve simulations a possible strategy could be to make a kinematic inversion up to higher frequencies ($2 - 5\ Hz$) and, to do

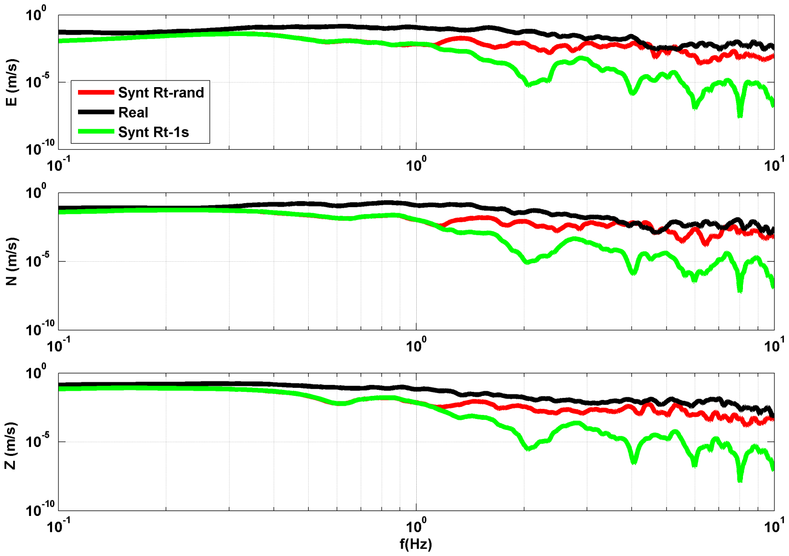

Figure 5.2.1: Velocity amplitude spectra for AQU station: real data (black); synthetic with $1s$ constant rise time (green); synthetic with ramdom rise time between $0.1s$ and $1s$ (red).

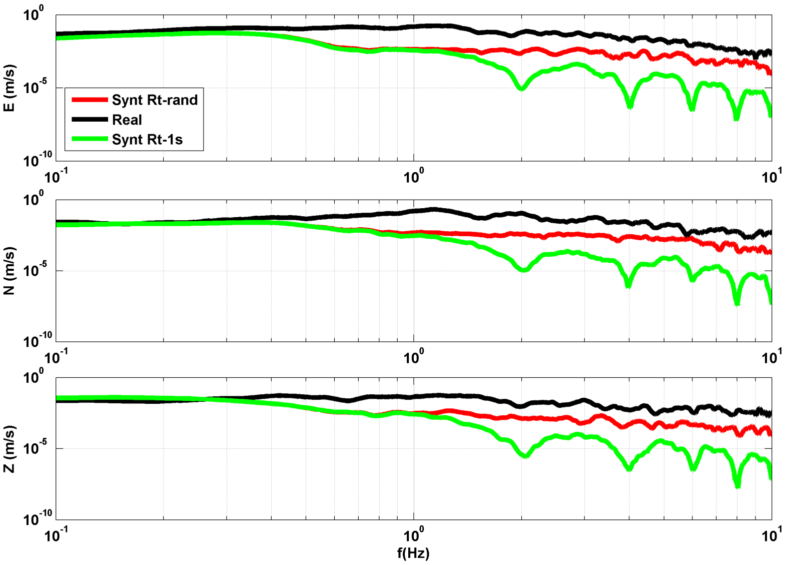

Figure 5.2.2: Same as Figure 5.2.1 for AQG station.

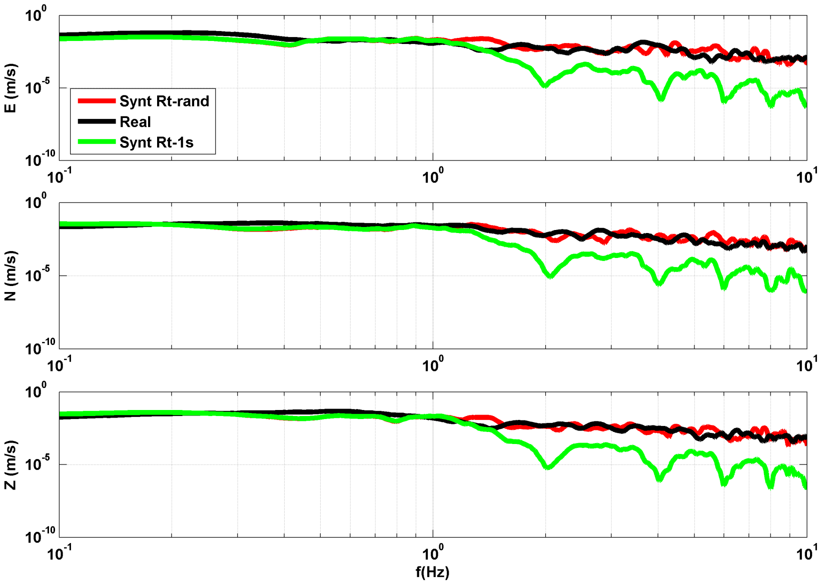

Figure 5.2.3: Same as Figure 5.2.1 for CLN station.

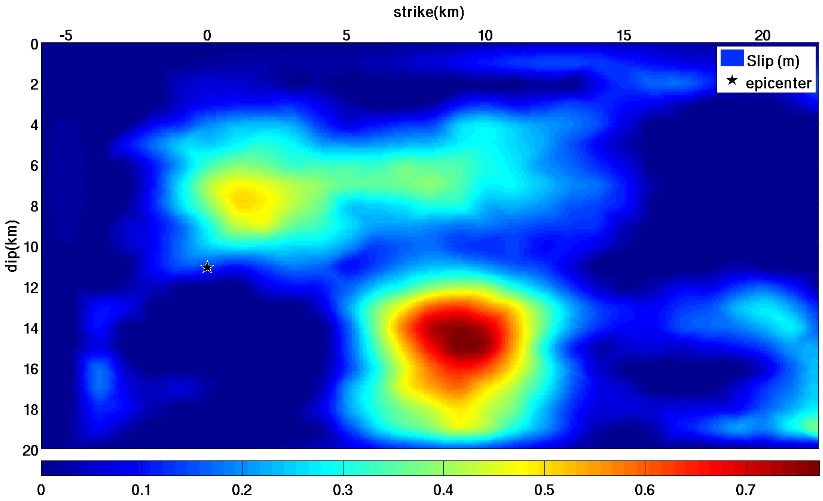

Figure 5.3.1: K^{-2} slip distribution obtained from the one in Figure 4.5.2.

that, we need to use a more detailed description of the propagation medium including also 3D and site effect maybe coupling numerical and empirical Green's functions directly in the inversion procedure.

5.4 Uncertainty due to the EGF selection

Results showed in the previous section are obtained describing the propagation effect at high frequencies with the selected EGFs of Table 3.2. In Figure 5.4.1 are indicated the positions of these EGFs over the fault plane. It is clear that they don't sample uniformly the fault surface and so we have associated, in the summation algorithm, at each subfaults simply the nearest one. It is reasonable to ask what is the influence of a particular EGF on the simulations and if it is actually better to use all of them toghether instead of one.

To investigate this aspect, we have done simulations varying the EGF one by one to show how the intrinsic variability of the EGFs corresponds to an epistemic uncertainty in the synthetics accelerograms and spectra. In Figure 5.4.2 and 5.4.3 are shown the comparisons between the accelerations for these simu-

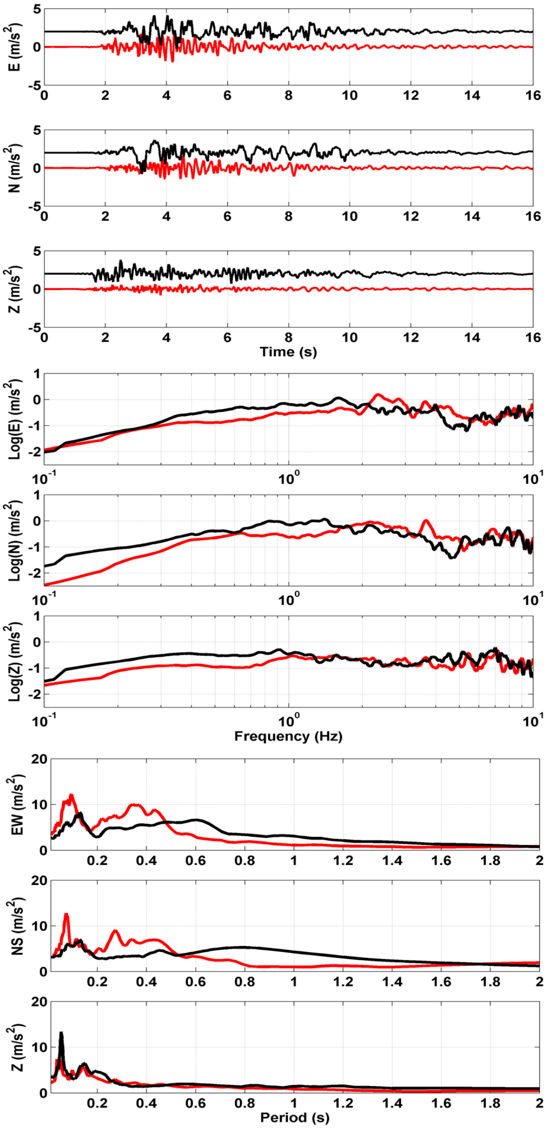

Figure 5.3.2: Acceleration waveform, amplitude spectra and response spectra for the station AQU. Synthetic data are plotted in red, whilst real ones in black. Real waveforms are shifted upward to facilitate comparison.

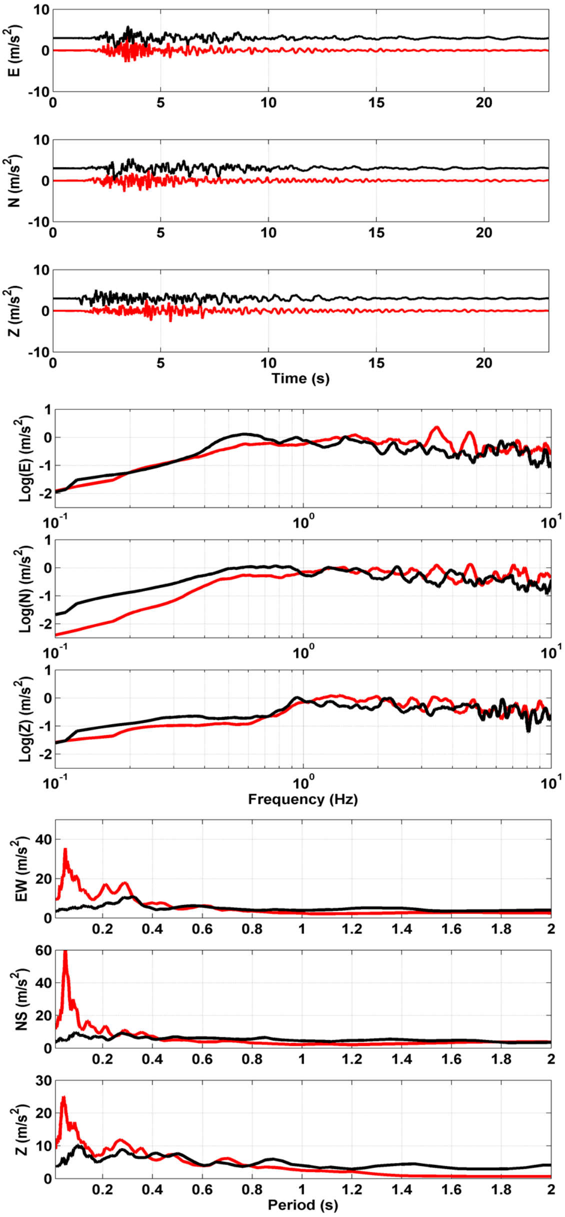

Figure 5.3.3: Same as Figure 5.3.2 for the station AQK.

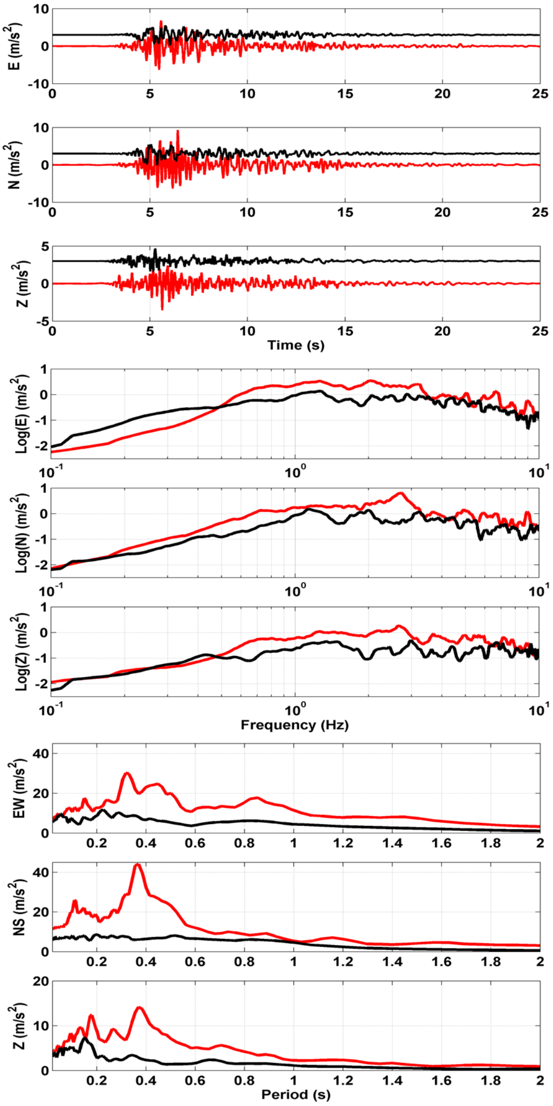

Figure 5.3.4: Same as Figure 5.3.2 for the station AQG.

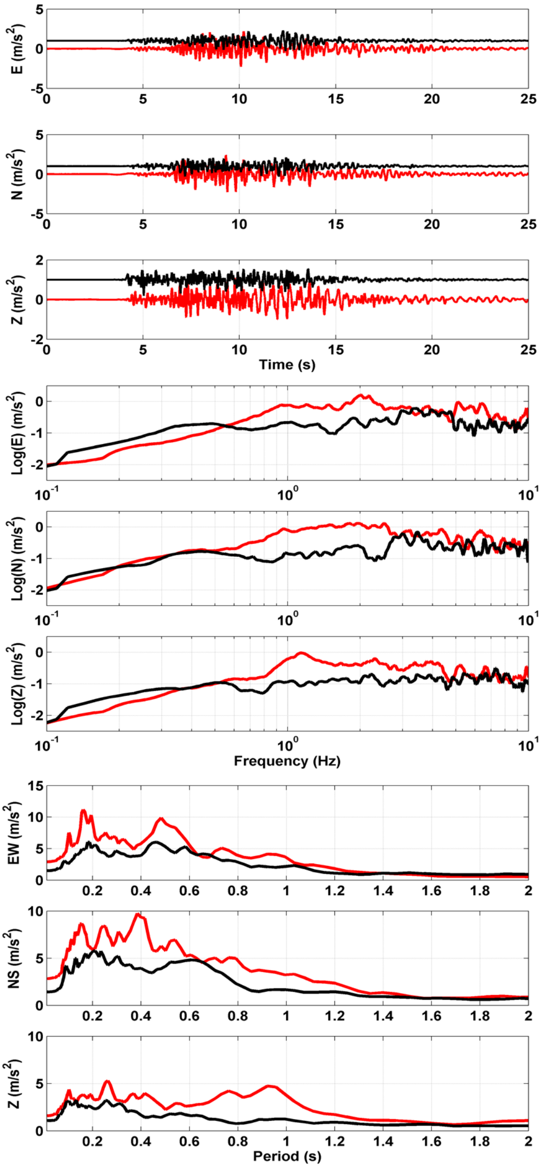

Figure 5.3.5: Same as Figure 5.3.2 for the station GSA.

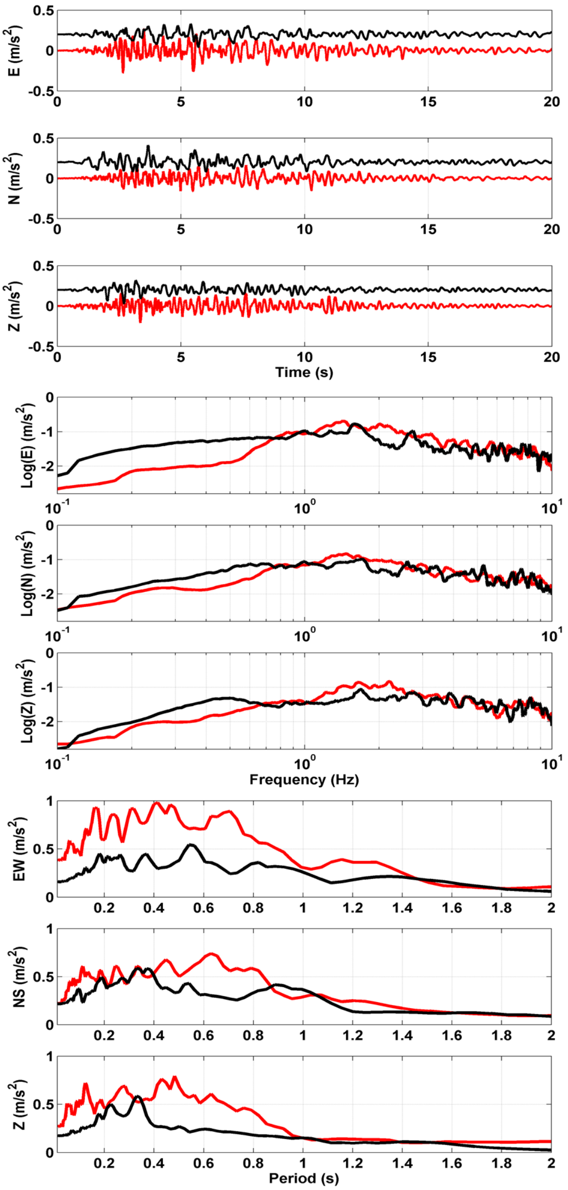

Figure 5.3.6: Same as Figure 5.3.2 for the station FMG.

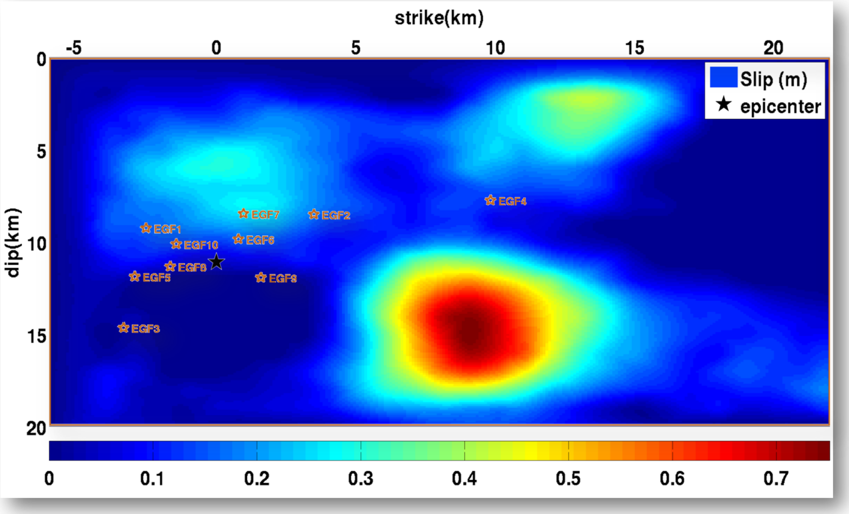

Figure 5.4.1: K^{-2} model used for the simulations and position of the selected EGFs over the fault plane.

lations and real data for two different stations: AQU, which is very close to the epicenter, located inside the projection of the fault plane on the surface; FMG, which is a bit far away from the fault (~25 km). We also made simulations using all the different EGFs together distributed over the fault plane. From now, we will refer to this two kind of configuration with "single-EGF" and "multiple-EGF". Using single-EGF configuration, results are strongly dependent to the particular aftershock chosen to approximate the propagation effect and to its position on the fault plane with respect to the station. The multiple-EGF configuration, instead, is a sort of average of all the empirical Green's functions but weighted by the way they sample the fault plane: after the discretization of the plane, as said before, we associate the nearest EGF to each subfault; because of the non uniform distribution of the events, we have that some regions (containing several subfaults) are associated to the same EGF and then, the simulations are more sensitive to those Green's functions that are much used in the summation algorithm.

In Figure 5.4.4 are then illustrated the comparisons between all the synthetics in terms of misfit between real and simulated Fourier amplitude acceleration spectra and also synthetic PGA values compared with real ones for the five stations considered in the previous section. Results show that the average effect of multiple-EGF configuration produces a significant improvement and, for this reason, we decided to adopt this configuration for the all simulations presented in this chapter.

5.5 Blind simulations

Our last goal is to build up a method to perform ground motion predictions in "blind" conditions, we want to perform simulations without any knowledge about the source process, except its magnitude and focal mechanism. We computed simulations using the same K^{-2} technique illustrated in the previous sections. To perform simulations without knowing exactly the source model, source parameters are randomly chosen from a priori probability density functions. In particular we focus our attention on roughness degree of slip heterogeneity (K value introduced in section 1.6), nucleation point position on the fault plane and rupture velocity (here considered as a constant over the fault plane). In agreement with the results obtained by Mai et al. (2005) and Causse et al. (2008), where they found probability density functions for the nucleation point along strike and dip directions (x_n, y_n) and rupture velocity v_r, and by Causse et al. (2010) for the distribution of the roughness parameter K, we perfomed

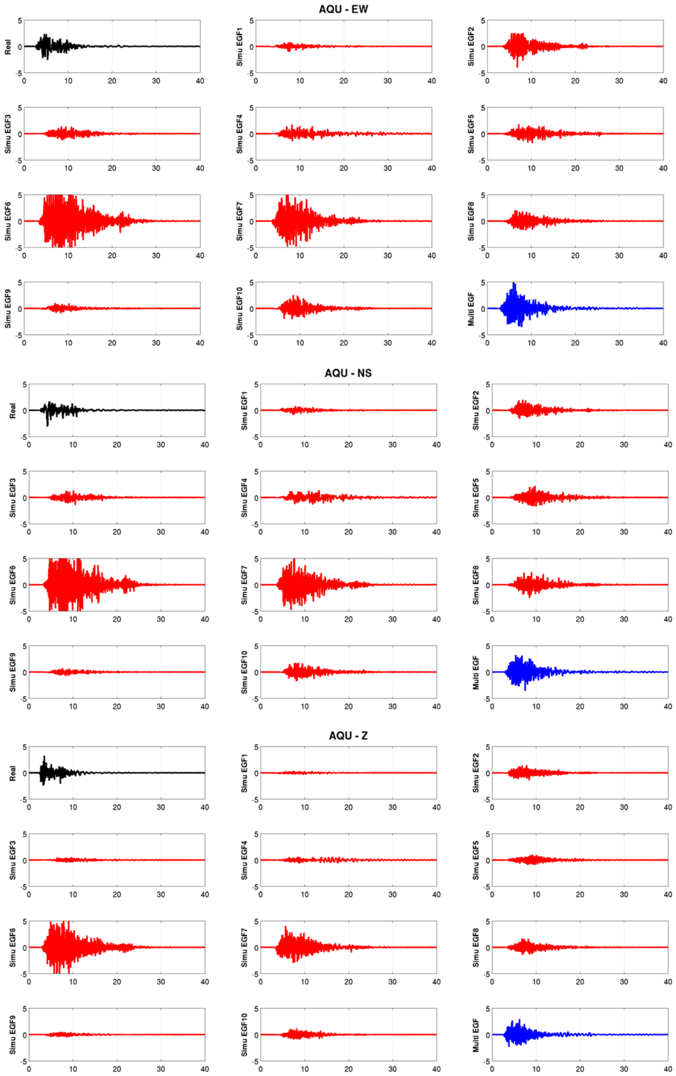

AQU - EW

AQU - NS

AQU - Z

Figure 5.4.2: Acceleration waveform for AQU station obtained using different EGFs: real data (black), single-EGF simulations (red) and multi-EGF simulation (blue).

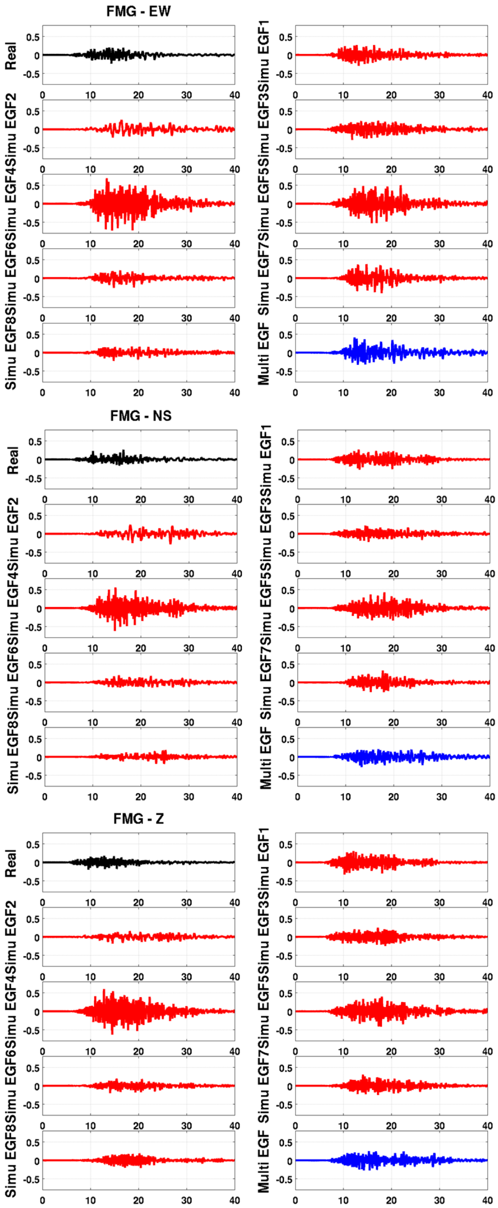

Figure 5.4.3: Same as Figure 5.4.2 for FMG station.

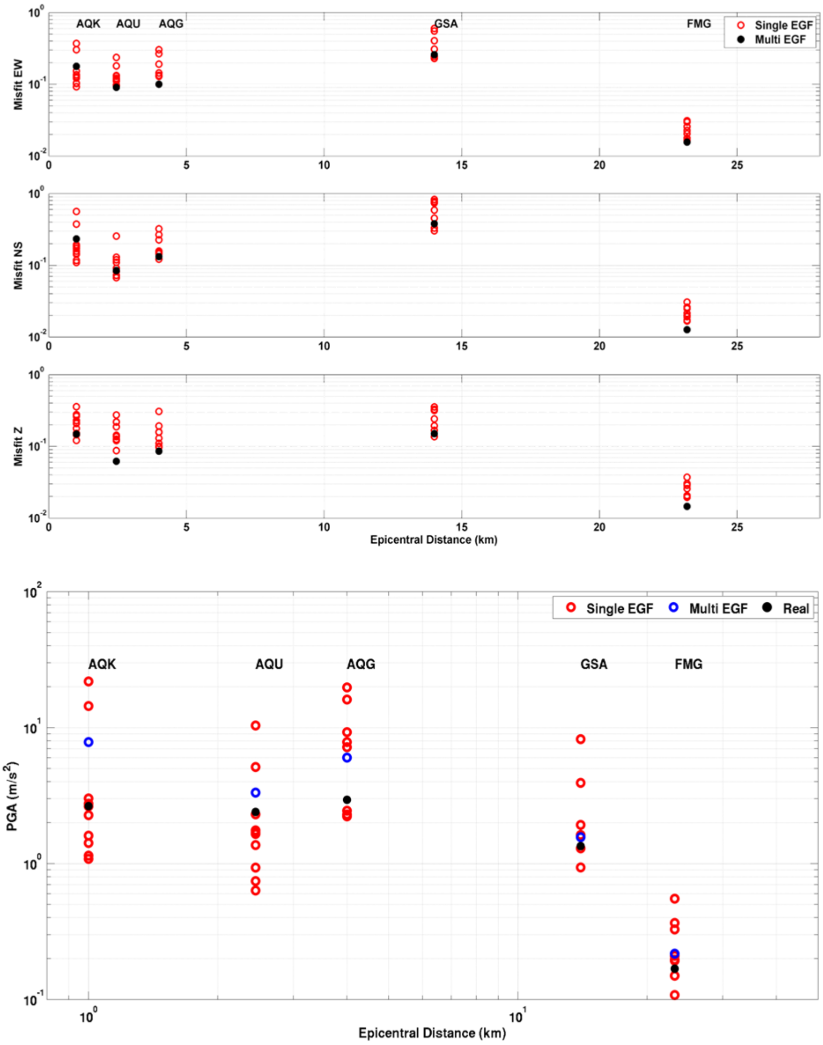

Figure 5.4.4: (Top) Misfit between real and synthetic amplitude acceleration spectra versus epicentral distance for the stations AQK, AQU, AQG, GSA and FMG. (Bottom) Real and synthetic PGA versus distance for the same stations.

100 simulations using the Latine Hypercube Sampling (LHS) method (McKay, 1988) to select for each parameter a set of values with respect to its distribution. Rupture velocity has a uniform distribution between 2.1 km/s and 2.7 km/s. Considering fault dimensions L and W normalized to 1, for x_n we used a normal distribution centered in 0.5 and with $\sigma = 0.23$. For y_n, instead, we used a Weibull distribution with a and b parameters respectively equal to 0.63 and 3.92. The choice of Weibull distribution is due to its non-simmetry, because we wanted to take into account that it's more probable to have nucleation at large depths instead of close to the surface. Roughness parameter is related to the stress drop and, in general, has a lognormal distribution (Causse et al., 2010) which depend on magnitude and fault dimensions

$$\log\left(\frac{K}{LW}\right) = 1.88 - 0.5M_W \tag{5.5.1}$$

For each station the median and standard deviation of the spectra were calculated and then compared with the real data. In Figures 5.5.1, 5.5.2 and 5.5.3 are shown the comparison between the simulations and real data in terms of acceleration Fourier and response spectra for AQG, AQU and FMG stations. To quantify the variability, we compute an average of the standard deviation of the spectra with respect to frequency (period for response spectra) and indicate it on the figures. Variability of the simulations is almost the same for all the stations because it mainly depends on the chosen a priori distributions of source parameters which are the same for all of them. Single simulations can be very different from the real data but, if we look at the average spectra, we see that there is a quite good agreement (in terms of trend and amplitude). Larger differencies are observed for near fault stations, in particular AQG for which we overestimate the low frequency part of the spectra. This can be due to

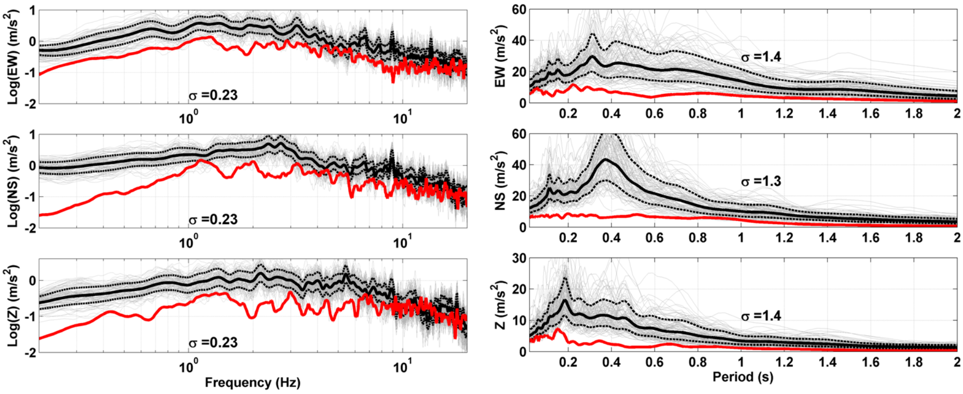

Figure 5.5.1: Blind simulations for AQG: single simulations (grey); mean and standard deviation of the spectra (continuous and dashed black lines); real data (red line). On the left panel we plotted the acceleration amplitude spectra, on the right panel the acceleration response spectra. Average standard deviation is indicated for each component.

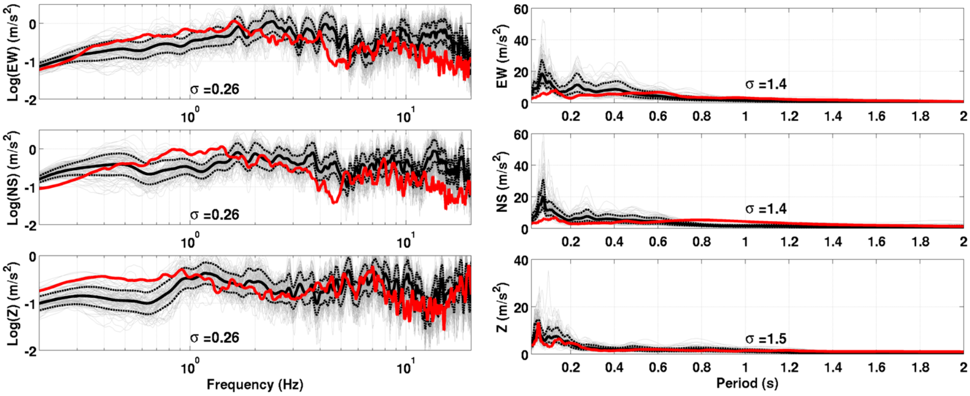

Figure 5.5.2: Same as previous Figure, but for AQU station.

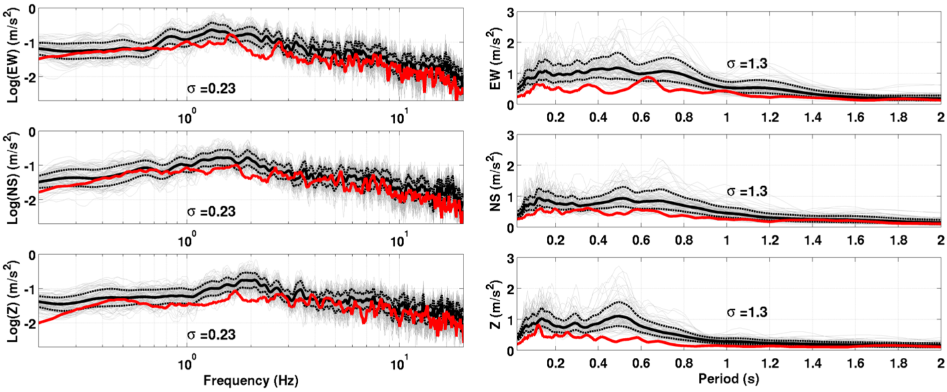

Figure 5.5.3: Same as previous Figure, but for FMG station.

Conclusions

In this work we illustrated a methodology to perform ground motion simulations giving a detailed description of the seismic source and the propagation effects. As a case test to validate the technique we investigated the 2009, L'Aquila earthquake, which is one of the best recorded earthquakes of the last years. Moreover a large amount of records in the vicinity of the source is available that could give us detailed information on the rupture process. Additionally, the large spatial variability of the ground motion in the epicentral area makes this earthquake an interesting case for testing performances of our simulation method.

To describe the source process, starting from the assumption of an extended fault, we need to choose a parametrization. Generally, source parameters that are important to kinematically characterize the rupture evolution are the final slip distribution, the rupture velocity (or rupture time)and the rise time. As a first step, we decided to fix the rise time and retrieve the final slip distribution and the rupture velocity from a kinematic inversion.We found the best model which is able to represent real observations at least in the frequency range [0.05-0.5 Hz] for that we have inverted them. It is a very smooth model, due to the adopted Gaussian slip parameterization and presents essentially three regions of non-zero slip, the largest one placed in the middle-bottom part of the fault and reaches the maximum value of about 1 m. We also showed, that is quite difficult to represent strong motion data in a wider frequency range because of the inadequate description of the propagation media at small scales by 1D velocity models, so that, kinematic inversions generally allows us to find a source model which is representative of a band-limited part of real ground motion. On the other hand, in numerical simulations the propagation medium contribution is commonly approximated by the Green's tractions computed using crustal velocity models obtained from tomographic inversions. Since these models are generally not so detailed, the propagation effect is band-limited too.

During an earthquake, the strong ground motion that is responsable of the damage to structures generally comes from high frequency acceleration picks; this is the reason for which we are interested in investigating the ground motion in a broader frequency range. High frequencies are related to small wavelengths, that is the set of phenomena that happen on the fault plane at a very small scale (few hundreds of meters). For this reason, we built up a technique to couple standard low frequency numerical simulations with high frequency simulations for which the propagation effect is described by Empirical Green's functions. This method quite well reproduces the high frequency content of records of stations far from the source but not for all the stations that are located very close to the fault, We tried to improve high frequency description considering a randomly variable rise time, but the high frequency content of the simulations is still reduced as compared to real data. Then, we integrated the description of the rupture process with a K-square model which reduced misfit between synthetics and observations both in far and near source conditions.

Another aspect that I investigated is the influence of the EGF selection of the ground motion simulation. I showed that simulations are very sensitive to peculiarity of a particular EGF and, to reduce this effect, it is better to make a good selection in terms of similarity to the main event and of signal to noise ratio. We showed that it is also better to use several EGF distributed over the plane instead of one, to make an average of the single propagation contributions, in particular this is true for the very near source stations.

At the end, we developed a technique to compute simulations without having a fixed source model. The idea is to have a method for performing ground motion predictions (in terms of acceleration waveform, amplitude spectra and response spectra) for a future earthquake starting from a priori source parameters probability density functions. We have tested also this technique for L'Aquila earthquake observing a good agreement between real data and the average of predictions both for amplitude and response acceleration spectra.

Synthetic seismograms are useful for the calculation of seismic hazard and for scenario predictions of future earthquakes. Since it is impossible to have real observations for any site of interest in active seismic zones, the possibility to use synthetics for seismic risk estimation and deterministic hazard analysis is really an important issue. Along this road, it is important to be sure of obtaining realistic signals which are representative of the source and propagation effects up to high frequencies. With this study we wanted to show the feasibility of computing realistic ground motion also without assuming specific knowledge of a source model. To perform a blind simulation we need to assume of knowing the position of the fault plane with respect to the site of interest, but not the source model, for which we can define a priori distribution of parameters. Although it is important to have very good quality records of small events, to use as EGFs, which are compatible with the source mechanism we are going to simulate. Having a dense network capable to register the background seismicity with an high signal to noise ratio can provide us a good dataset of empirical Green's functions.

Bibliography

[1] Aki, K., Richards, P.G., 2002. Quantitative Seismology, Freeman and Co., New York.

[2] G. Ameri, F. Gallovič, and F. Pacor. Complexity of theMw6.3 2009 L'Aquila (central Italy) earthquake: 2. Broadband strong motion modeling. JOURNAL OF GEOPHYSICAL RESEARCH, VOL. 117, B04308, doi:10.1029/2011JB008729, 2012

[3] Atzori S., Hunstad I., Chini M., Salvi S., Tolomei C., Bignami C., Stramondo S., Trasatti E., Antonioli A. and Boschi E.; 2009: Finite fault inversion of DInSAR coseismic displacement of the 2009 L'Aquila earthquake (central Italy). Geophys. Res. Lett., 36, L15305-L15311, doi: 10.1029/2009GL039293.

[4] Boncio P., Lavecchia G., and Pace B.; 2004: Defining a model of 3D seismogenic sources for seismic hazard assessment applications: the case of central Apennines (Italy). J. Seismol., 8, 407- 425, doi: 10.1023/B: JOSE.0000038449.78801.05.

[5] Bouchon, M., 1981. A simple method to calculate Green's functions for elastic layered media, Bull. Seism. Soc. Am., 71, 959-977.

[6] Causse, M., Chaljub, E., Cotton, F., Cornou, C. and Bard, P.-Y. (2009), New approach for coupling k−2 and empirical Green's functions: application to the blind prediction of broad-band ground motion in the Grenoble basin. Geophysical Journal International, 179: 1627–1644.

[7] Cavinato G.P. and De Cellis P.G.; 1999: Extensional basins in the tectonically bimodal central Apennines fold-thrust belt, Italy: response to corner flow above a subduction slab in retrograde motion. Geology, 27, 955-958.

[8] Chaljub, E., Komatitsch, D., Vilotte, J.-P., Capdeville, Y., Valette, B., Festa, G., 2007. Spectral element analysis in seismology, in Advances in Wave Propagation in Heterogeneous Media, 48, 365–419, eds Wu, R., and Maupin, V., Advances in Geophysics, Elsevier - Academic Press.

[9] Chiarabba, C., Bagh, S., Bianchi, I., De Gori, P. & Barchi, M., 2010. Deep structural heterogeneities and the tectonic evolution of the Abruzzi region (Central Apennines, Italy) revealed by microseismicity, seismic tomography, and teleseismic receiver functions, Earth planet. Sci. Lett., 295, 462–476, doi:10.1016/j.epsl.2010.04.028

[10] Chiaraluce, L. et al., 2011a. The 2009 L'Aquila (Central Italy) seismic sequence, Bollettino di Geofisica Teorica e Applicata, 52(3), doi:10.4430/bgta0019.

[11] Cirella, A., Piatanesi, A., Cocco, M., Tinti, E., Scognamiglio, L., Michelini, A., Lomax, A. & Boschi, E., 2009. Rupture history of the 2009 L'Aquila earthquake from non-linear joint inversion of strong motion and GPS data, Geophys. Res. Lett., 36, L19304, doi:10.1029/2009GL039795.

[12] A. Cirella, A. Piatanesi, E. Tinti, M. Chini and M. Cocco. Complexity of the rupture process during the 2009 L'Aquila, Italy, earthquake. Geophys. J. Int. (2012) 190, 607–621

[13] Cotton F. and Campillo M. (1995). Frequency domain inversion of strong motion: application to the 1992 Landers earthquake, J. Geophys. Res. 100, 3961-3975.

[14] Coutant, O., 1989. Programme de simulation numérique AXITRA, Rapport LGIT, Université Joseph Fourier, Grenoble, France.

[15] Crosson, R.S., 1976. Crustal structure modelling of earthquake data. Simultaneous least squares estimation of hypocentre and velocity parameters, J. geophys. Res, 81, 3036–3046.

[16] Di Stefano, R., Chiarabba, C., Chiaraluce, L., Cocco, M., De Gori, P., Piccinini, D. & Valoroso, L., 2011. Fault zone properties affecting the rupture evolution of the 2009 (Mw 6.1) L'Aquila earthquake (Central Italy): insights from seismic tomography, Geophys. Res. Lett., 38, L10310, doi:10.1029/2011GL047365.

[17] Dumbser, M., Käser, M., 2006. An Arbitrary High Order Discontinuous Galerkin Method for Elastic Waves on Unstructured Meshes II: The Three-Dimensional Isotropic Case, Geophys. J. Int., 167,(1), 319-336, doi:10.1111/j.1365-246X.2006.03120.x.

[18] Ellsworth, W. & Chiaraluce, L., 2009. Supershear during nucleation of the 2009 Mw 6.3 L'Aquila, Italy Earthquake. EOS, Trans. Am. geophys. Un., 90(52), Fall Meet. Suppl., Abstract U13C-07.

[19] Emolo A. (2002), Modelli di frattura dei terremoti crostali di media e forte magnitudo dall'inversione non lineare di registrazioni a corto periodo, Ph. D. Thesis, Univ. Napoli "Federico II".

[20] G. Festa and A. Zollo From data to source parameters: Kinematic modeling (2012). In "The mechanics of Faulting: From Laboratory to Real Earthquakes" , Eds: Andrea Bizzarri & Harsha S. Bhat ISBN: 978-81-308-0502-3, Research Signpost 37/661 (2), Fort P.O. Trivandrum-695 023 Kerala, India

[21] Fukuyama E., Irikura K. (1986). Rupture process of the 1983 Japan Sea (Akita-Oki) earthquake using a waveform inversion method, Bull. Seism. Soc. Am. 76, 1623-1640.

[22] Fukuyama, E. and T. Mikumo (1993). Dynamic rupture analysis: Inversion for the source process of the 1990 Izu-Oshima, Japan, earthquake (M 6.5), J. Geophys. Res., 98, 6529-6542.

[23] Galadini F. and Galli P.; 2000: Active tectonics in the central Apennines (Italy)-input data for seismic hazard assessment. Nat. Hazards, 22, 225-270.

[24] Gallovič F., Brokesova J. (2004). On strong ground motion with k-2 slip distribution, Journal of Seism. 211-221.

[25] Gerver and Markushevich (1966

[26] Graves, R.W., 1996. Simulating seismic wave propagation in 3D elastic media using staggered-grid finite differences, Bull. Seism. Soc. Am., 86, (4), 1091-1106.

[27] Graves, R.W., Wald, D.J., 2001. Resolution analysis of finite fault source inversion using one- and three-dimensional Green's functions: 1. Strong motions, J. Geophys. Res., 106, 8745– 8766.

[28] Guatteri, M., P. M. Mai, G. C. Beroza, and J. Boatwright (2003). Strong ground-motion prediction from stochastic-dynamic source models, Bull. Seism. Soc. Am., 93, 301-313.

[29] Herrero, A. & Bernard, P., 1994. A kinematic self-similar rupture process for earthquakes, Bull. seism. Soc. Am., 84, 1216–1228.

[30] Heaton, T. H. (1990). Evidence for and implications of self-healing pulses of slip in earthquake rupture, Phys. Earth Planet, Int. 64, 1- 20.

[31] Hisada Y., (2000). A theoretical omega-square model considering the spatial variation on slip and rupture velocity, Bull. Seism. Soc. Am., 90, 387-400.

[32] Hisada Y., (2001). A theoretical omega-square model considering the spatial variation on slip and rupture velocity. II. Case for a twodimensional source model, Bull. Seism. Soc. Am., 91, 651-666.

[33] Hunstad I., Selvaggi G., D'Agostino N., Englaand P., Clarke P. and Pierozzi M.; 2003: Geodetic strain in peninsular Italy between 1875 and 2001. Geophys. Res. Lett., 30, 1181-1185.

[34] Hutchings, L., 1994. Kinematic earthquake models and synthesized ground motion using empirical, Green's functions, Bull. Seism. Soc. Am., 84, (4), 1028-1050.

[35] Hutchings, L., Wu, F., 1990. Empirical Green's functions from small earthquakes: a waveform study of locally recorded aftershocks of the San Fernando earthquake, J. Geophys. Res., 95, 1187-1214.

[36] Irikura, K., 1983. Semi-empirical estimation of strong ground motions during large earthquakes, Bull. Disas. Prev. Res. Inst., 33, 63-104.

[37] Jeffreys H., Jeffreys B.S. (1972). Methods of Mathematical Physics, 3rd ed., Cambridge: Cambridge University Press

[38] Judenherc, S., and A. Zollo (2004), The Bay of Naples (southern Italy): Constraints on the volcanic structures inferred from a dense seismic survey, J. Geophys. Res., 109, B10312, doi:10.1029/2003JB002876.

[39] Kennett, B.L.N., Kerry, N.J., 1979. Seismic waves in a stratified half-space, Geophys. J. Royal Astr. Soc., 57, 557–583.

[40] Kissling E., W. L. Ellsworth, D. Eberhart-Phillips and U. Kradolfer, Initial reference models in local earthquake tomography, JOURNAL OF GEOPHYSICAL RESEARCH, VOL. 99, NO. B10, PAGES 19,635-19,646, OCTOBER 10, 1994.

[41] Kissling, E., 1995. Velest User's Guide. Internal Report, 26 pp., Institute of Geophysics, ETH Zurich

[42] Komatitcsh, D., Vilotte, J.-P., 1998. The Spectral element method: an efficient tool to simulate the seismic response of 2D and 3D geological structures, Bull. Seism. Soc. Am., 88, (2), 368-392.

[43] Lavecchia G., Brozzetti F., Barchi M., Keller J. and Menichetti M.; 1994: Seismotectonic zoning in east-central Italy deduced from the analysis of the Neogene to present deformations and related stress fields. Geol. Soc. Amer. Bull., 106, 1107-1120.

[44] Lawson C. L. and Hanson, B. J. (1974). Solving Least Squares Problems, Prentice-Hall (Englewood Cliffs, NJ).

[45] Lay, T., & Wallace, T. C. 1995, Modern Global Seismology (New York: Academic)

[46] Liu, P., Archuleta, R.J., 2004. A new nonlinear finite fault inversion with three-dimensional Green's functions: Application to the 1989 Loma Prieta, California, earthquake, J. Geophys. Res., 109, B02318, doi:10.1029/2003JB002625.

[47] E. Lucca, G. Festa, and A. Emolo Kinematic Inversion of Strong Motion Data Using a Gaussian Parameterization for the Slip: Application to the 2008 Iwate–Miyagi, Japan, Earthquake Bulletin of the Seismological Society of America December 2012 102:2685-2703.

[48] Lucente, F.P., Gori, P.D., Margheriti, L., Piccinini, D., Bona, M.D., Chiarabba, C. & Piana Agostinetti, N., 2010. Temporal variation of seismic velocity and anisotropy before the 2009 MW 6.3 L'Aquila earthquake, Italy, Geology, 38, 1015–1018, doi:10.1130/G31463.1.

[49] Moczo, P., Lucka, M., Kristek, J., Kristekova, M., 1999. 3D Displacement finite differences and a combined memory optimization,BullSeismSocAm 89, (1), 69 - 79.

[50] Montone P., Mariucci M.T., Pondrelli S. and Amato A.; 2004: An improved stress map for Italy and surrounding regions (central Mediterranean). Jour. Geophys. Res., 109, B10410-B10432, doi: 10.1029/ 2003JB002703

[51] Müller, G., 1985. The reflectivity method: a tutorial, J. Geophys., 58, 153–174.

[52] NELDER S. L. S. and R. MEAD, A Simplex method for function minimization, Computer Journal, 7,308, 1965.

[53] Numerical Recipes in Fortran 77, Second Edition (1992).

[54] Olson A. H. and Apsel R. J. (1982). Finite faults and inverse theory with application to the 1979 Imperial Valley earthquake, Bull. Seism. Soc. Am. 72, 1969-2001.

[55] Olson, A.H., Orcutt, J.A., Frazier, G.A., 1984. The discrete wavenumber/finite element method for synthetic seismograms, Geophys. J. Royal Astr. Soc., 77, 421–460, doi: 10.1111/j.1365-246X.1984.tb01942.x.

[56] Sambridge M. (1999). Geophysical inversion with a Neighbourhood algorithm I: searching a parameter space, Geophys. J. Int. 138, 479-494.

[57] Sambridge M. (2001). Geophysical inversion with a Neighbourhood algorithm II: appraising the ensemble, Geophys. J. Int. 138, 727-746.

[58] Scognamiglio L., Tinti E., Michelini A., Dreger D.S., Cirella A., Cocco M., Mazza S. and Piatanesi A.; 2010: Fast determination of moment tensors and rupture history: what has been learned from the 6 April 2009 L'Aquila earthquake sequence. Seism. Research Lett., 81, 892-906, doi: 10.1785/gssrl.81.6.892.

[59] Spudich, P., Xu, L.S., 2003. Software for calculating earthquake ground motions from finite faults in vertically varying media, International Handbook of Earthquake & engineering seismology (Edi. W.H.K. Lee, H. Kanamori, P.C. Jennings, C. Kisslinger), Academic Press, Part B, 1857-1875.

[60] Thurber, CH., 1992. Hypocentre–velocity structure coupling in local earthquake tomography, Phys. Earth planet. Inter., 75, 55–62.

[61] Ward S.N. and Valensise G.R.; 1989: Fault parameters and slip distribution of the 1915 Avezzano, Italy, earthquake derived from geodetic observations. Bull. Seismol. Soc. Am., 79, 690-710.

[62] Zhu, L., Rivera, L., 2001. Computation of dynamic and static displacement from a point source in multi-layered media, Geophys. J Int., 148, 619–627.

[63] Zollo, A., et al. (2003), Evidence for the buried rim of Campi Flegrei caldera from 3-D active seismic imaging, Geophys. Res. Lett., 30(19), 2002, doi:10.1029/2003GL018173.

[64] Zollo, A. and Emolo, A. Terremoti e onde. Metodi e pratica della sismologia moderna, (2011) Liguori Editore.

[65] A. Zollo, N. Maercklin,M. Vassallo, D. Dello Iacono, J. Virieux, and P. Gasparini Seismic reflections reveal a massive melt layer feeding Campi Flegrei caldera (2008). Geophys.Res.Lett. 35, LXXXXX, doi:10.1029/2008GL034242

List of Figures

1.2.1 Representation of a seismic fault as a surface inside a volume V along which slip occurs (Festa and Zollo, 2012). 13

1.2.2 Double couple equivalent system for a vertical strike slip fault. The pressure and traction along principal axes is also shown with the relative generated radiation pattern for P and S waves. (Zollo and Emolo, “Terremoti e Onde”) 14

1.2.3 Approximation of a real rupture process with an equivalent double couple force system (Lay and Wallace, 1995, “Modern Global Seismology”). 15

1.2.4 Representation of fault geometry and spatial orientation (Aki and Richards, 2002, “Quantitative Seismology”). 16

1.4.1 shape of rectangular and triangular source time function (left) and their amplitude spectra (right) 19

1.5.1 The same slip map represented by different parametrizations. On the left, a constant cell discretization, in the middle, a bi-cubic spline interpolation based on control nodes, on the right a superposition of overlapping Gaussian functions. The two smooth images are very similar, with differences related to the shape of the singularities (Festa and Zollo, 2012). 21

1.5.2 Example of slip distribution obtained by overlapping of 2D Gaussian functions. 22

1.5.3 Example of exploration for two parameters problem. The upper-left panel shows 10 samples and the corresponds Voronoi cells; the upper-right panel shows 100 samples. The lower-left panel similar to upper-right panel but with 10000 samples. Here the algorithm concentrates on four distinct region corresponding to the minimum of the misfit. The lower-right panel shows the contours of the misfit function in grey scale. 24

1.6.1 Representation of the rupture process, modelled as a slip pulse propagating at constant rupture velocity v. The figure also displays example of resulting STFs, compared with the functions that would be obtained from a classical k^{-2} model (without random nucleation points). (Causse et al., 2009) 26

2.2.1 P-wave, S-wave and near field computed for: $r = 10km$, $c_p = 5km/s$, $c_s = 3km/s$, $\rho = 2.5g/cm^3$, $\gamma_i = \gamma_j = \frac{1}{\sqrt{2}}$. 30

2.4.1 Geometry of the ray segment ds, along a path from a source to a surface receiver. The velocity of the medium varies only along the z direction, so there will be symmetry of downgoing and upgoing legs of the raypath. 35

2.4.2 Possible outcomes for a step in the downhill simplex method. The simplex at the beginning of the step, here a tetrahedron, is shown, top. The simplex at the end of the step can be any one of (a) a reflection away from the high point, (b) a reflection and expansion away from the high point, (c) a contraction along one dimension from the high point, or (d) a contraction along all dimensions towards the low point. An appropriate sequence of such stepswill always converge to a minimum of the function. (Numerical Recipes, 1992) 39

2.4.3 Sources (red stars) and receivers (blue triangles) positions and ray paths considered in the synthetic test. 40

2.4.4 Velocity distribution versus depth for the starting models defining the initial simplex (grey lines), the “true” model (red line) and the final one obtained from the inversion (blue line). 41

2.4.5 Map of the SERAPIS survay: airgun shots (grey dots), seismic stations and seabottom receivers (triangles). Considered station is circled in red. 42

2.4.6 Selected 272 travel times used for the inversion procedure (black dots) versus distance from OBS-9. Blue dots are relative to all 2000 first P arrival times measured on traces recorded by this receiver. 44

2.4.7 Geophysical and structural model of the deep structure of the Campi Flegrei caldera. (a) Average 1-D P-velocity model for the Campi Flegrei caldera, based on PP and PS travel times, and on PS-to-PP amplitude ratios. The dashed line is the average of the 3-D P-velocity model in the study area. (b) Vp/Vs ratio as a function of depth, as estimated in the present study. The dotted lines are two Vp/Vs depth profiles that were estimated from the local earthquake tomography (Vanorio et al., 2005). C: Stratigraphic model. D: Geological sketch model of the Campi Flegrei caldera. (from Zollo et al., 2008). 45

2.4.8 Initial models (interpolated by cubic splines) for starting simplex (gray line) and comparison between final best model (red line) and the one proposed by Zollo et al., 2008 for the Pozzuoli bay (blue line). 46

3.2.1 Map of the seismogenic areas for the Umbria-Marche-Abruzzo Apennines and epicentres of historical earthquakes larger than $VIII$ on the MCS scale ($M \geq 5.7$) from C.P.T.I. catalogue (Working Group CPTI, 1999); dates refer to the year of earthquake occurrence (from Boncio et al., 2004). 51

3.3.1 PGA and PGV shakemaps computed by INGV few days after the main event using all available data. 52

3.5.1 Earthquake self-similarity: we observe a constant stress-drop scaling of source parameters. 55

3.5.2 Map of the L'Aquila 2009 seismic sequence. Epicenters (from 2008/12/01 to 2009/11/30) are shown using gray dots. The focal mechanisms determined using the TDMT technique are shown as beach balls with different colors depending on M_W. The mainshock mechanism is in red. (From Scognamiglio et al., 2010). . . 56

3.5.3 Distribution of sigma versus distance for different stations. 58

4.2.1 Map of all the avalaible stations at regional scale which have recorded the mainshock. 61

4.4.1 The figure shows the normalized misfit between real and synthetic data as function of the rupture velocity. 63

4.4.2 Final slip distribution obtained by inversion for a constant rupture velocity, $v_r = 3.5\,km/s$. 64
4.4.3 Synthetic ground displacement (red dashed lines) compared with real ones (black lines) for all the inverted stations. Data are shown in the frequency range used for the inversion: $0.05 - 0.3\,Hz$. 65
4.5.1 Smallest misfit per iteration between synthetics and observations as a function of number of iterations. Red line indicates the minimum value obtained for a constant rupture velocity ($v_r = 3.5\,km/s$). 66
4.5.2 Best source model obtained from kinematic inversion in terms of slip distribustion (in color) and isolines of constant rupture time. 67
4.5.3 Synthetic ground displacement (red dashed lines) obtained with the model in Figure 4.5.2 compared with real ones (black lines) for all the inverted stations. 68
4.5.4 Slip map and rupture time isolines obtained from kinematic inversion with data selected in the frequency range $0.05 - 0.7\,Hz$. . 69
4.5.5 Synthetic ground displacement (red dashed lines) compared with real ones (black lines) for all the inverted stations. Data are shown in the frequency range used for the inversion: $0.05 - 0.7\,Hz$. 70
4.5.6 Comparison between misfit values versus number of iteration for two inversions made considering two different frequency range: $0.05 - 0.3\,Hz$ (in red) and $0.05 - 0.7\,Hz$ (in black). 71

5.1.1 Schematic representation of the method used for coupling low and high frequency simulations. 74
5.2.1 Velocity amplitude spectra for AQU station: real data (black); synthetic with $1s$ constant rise time (green); synthetic with ramdom rise time between $0.1s$ and $1s$ (red). 76
5.2.2 Same as Figure 5.2.1 for AQG station. 77
5.2.3 Same as Figure 5.2.1 for CLN station. 78
5.3.1 K^{-2} slip distribution obtained from the one in Figure 4.5.2. . . . 79
5.3.2 Acceleration waveform, amplitude spectra and response spectra for the station AQU. Synthetic data are plotted in red, whilst real ones in black. Real waveforms are shifted upward to facilitate comparison. 80
5.3.3 Same as Figure 5.3.2 for the station AQK. 81
5.3.4 Same as Figure 5.3.2 for the station AQG. 82
5.3.5 Same as Figure 5.3.2 for the station GSA. 83
5.3.6 Same as Figure 5.3.2 for the station FMG. 84

5.4.1 K^{-2} model used for the simulations and position of the selected EGFs over the fault plane. 85
5.4.2 Acceleration waveform for AQU station obtained using different EGFs: real data (black), single-EGF simulations (red) and multi-EGF simulation (blue). 87
5.4.3 Same as Figure 5.4.2 for FMG station. 88
5.4.4 (Top) Misfit between real and synthetic amplitude acceleration spectra versus epicentral distance for the stations AQK, AQU, AQG, GSA and FMG. (Bottom) Real and synthetic PGA versus distance for the same stations. 89
5.5.1 Blind simulations for AQG: single simulations (grey); mean and standard deviation of the spectra (continuous and dashed black lines); real data (red line). On the left panel we plotted the acceleration amplitude spectra, on the right panel the acceleration response spectra. Average standard deviation is indicated for each component. 91
5.5.2 Same as previous Figure, but for AQU station. 91
5.5.3 Same as previous Figure, but for FMG station. 92

List of Tables

3.1 Model based on Bianchi et al. (2010) V_S profile for station FAGN. V_P values are computed adopting a $V_P/V_S = 1.86$ (Ameri et al., 2012). 54
3.2 Magnitudes and focal mechanisms for the mainshock and the 10 selected aftershocks 57

4.1 Listi of selected stations with thei geographycal location and epicentral distance. 60